Chemical Engineering Journal 485 (2024) 149526

Contents lists available at ScienceDirect

Chemical Engineering Journal

journal homepage: www.elsevier.com/locate/cej

Plasma treatment of electrodeposited Sb_2Se_3 thin films for improvement of solar-driven hydrogen evolution reaction

Magno B. Costa [a,1], Moisés A. de Araújo [b,1], Robert Paiva [a], Sandra A. Cruz [a], Lucia H. Mascaro [a,*]

[a] Departamento de Química, Universidade Federal de São Carlos, Rodovia Washington Luiz, km 235, zip code: 13565-905, São Carlos – São Paulo, Brazil
[b] Instituto de Química de São Carlos, Universidade de São Paulo, Avenida Trabalhador Sancarlense, 400, zip code: 13566-590, São Carlos – São Paulo, Brazil

ARTICLE INFO

Keywords:
Antimony selenide
Hydrogen
Plasma treatment
Surface modification
Wettability
Water splitting

ABSTRACT

Semiconductor films based on Sb_2Se_3 are a promising choice to be applied as photocathodes for H_2 generation via solar-driven water splitting. However, the surface of Sb_2Se_3 is extremely hydrophobic, which considerably compromises its photoelectrochemical (PEC) performance. To tackle this issue and improve H_2 generation via light-driven water splitting, we have developed a plasma treatment approach and evaluated the effect of plasma type (i.e., plasma of N_2 and ambient air) and plasma exposure time. According to water contact angle measurements, the surface of the Sb_2Se_3 films changed from hydrophobic to hydrophilic over increasing plasma treatment time, and that was noticed for both N_2 and ambient air plasmas. XPS analyses showed the formation of a new Sb–N bond on the surface of the plasma-treated Sb_2Se_3 and this may have enhanced wettability since the N in the Sb–N bond has the propensity to form hydrogen bonds with water. The PEC analyses showed that the optimized plasma treatment condition (N_2 plasma for 20 s) of the Sb_2Se_3 films delivered a substantial photocurrent density (j_{ph}) value for HER of (–3.9 ± 0.3) mA cm^{-2} at −0.2 V_{RHE}, i.e., corresponding to 3-fold increase compared to that of the untreated film. Based on additional physical and electrochemical characterizations, the improved PEC performance for HER was assigned to the combined contribution of enhanced wettability and enlarged ECSA of the plasma-treated Sb_2Se_3 films. Overall, this work features a new and simple method based on plasma treatment to improve the wettability of those semiconductor films facing hydrophobicity and to enhance solar-driven water splitting.

1. Introduction

The use of oil for energy supply has become one of the most important products in the economic and geopolitical scenarios around the world. However, oil or fossil fuels often feature increases and volatility in prices, and on top of that, the exhaustive burning of this non-renewable resource for energy purposes causes very serious environmental impacts. To exemplify, the excessive emission of carbon dioxide released into the atmosphere from fossil fuels has contributed to the intensification of the greenhouse effect and climate change, being the main responsible for global warming and environmental damage. To circumvent these problems, efforts have been made to develop technologies that could replace fossil fuels in favor of using renewable energy sources available on our planet, such as the sun, as it can provide more than enough energy to meet all the global energy demand.

One way to harvest solar energy is via using photoelectrochemical (PEC) cells, which deal with the conversion of solar energy into chemical energy, that can generate hydrogen gas (H_2), i.e., clean energy carriers, from photoelectrolysis of water (also known as solar-driven water splitting) [1]. Among the semiconductor materials under consideration for H_2 generation in PEC cells, films based on antimony(III) selenide (Sb_2Se_3) are an excellent choice of semiconductor due to the adequate optoelectronic properties of this material [2] as well as the low-toxicity and the abundance of Sb_2Se_3's chemical elements [3,4]. In terms of optoelectronic properties, Sb_2Se_3 features a high absorption coefficient (α) of $\geq 10^5$ cm^{-1} in the ultraviolet and visible region of the solar spectrum [5], suitable optical bandgap energy (E_g) of 1.10–1.17 eV [6,7], whose values enable a theoretical maximum photocurrent density (j_{ph}) of > 38 mA cm^{-2} [8], and proper energy position of the conduction band for the occurrence of hydrogen evolution reaction (HER) [9]. Another advantage of Sb_2Se_3 is that this material has only one single crystalline phase [10], consisting of stacked one-dimensional parallel

* Corresponding author.
E-mail address: lmascaro@ufscar.br (L.H. Mascaro).
[1] These authors contributed equally to this work.

https://doi.org/10.1016/j.cej.2024.149526
Received 22 November 2023; Received in revised form 27 January 2024; Accepted 7 February 2024
Available online 20 February 2024

$(Sb_4Se_6)_n$ ribbons (formed by trigonal and tetragonal polyhedra $Sb_1Se_2Se_3$ linked alternately [3]). This crystal structure exhibits anisotropic behavior for charge carriers transportation, i.e., photogenerated charge carriers travel more efficiently along the $(Sb_4Se_6)_n$ ribbons compared to their transportation between ribbons (hopping transport mechanism) [11–13]. Studies have shown that preferential crystal growth of Sb_2Se_3 films at the [*hk1*] direction can provide a better transportation of the photogenerated charge carriers [14–16]. For example, a recent study reported the obtainment of [*hk1*]-oriented Sb_2Se_3 films in a multilayer-based photocathode, namely, Mo/Sb_2Se_3/CdS(In)/TiO_2/Pt, and this system delivered a substantial cathodic j_{ph} of -35.7 mA cm^{-2} at 0 V_{RHE}, onset potential of 0.54 V_{RHE} and half-cell solar-to-hydrogen conversion efficiency of 5.6 % [17]. Sb_2Se_3 semiconductor has also gained interest and has been widely investigated over the past years as a light-harvesting material for photovoltaic [18] and photodetector technologies [19], reaching high efficiency and performance [20,21].

It is fair to mention that Sb_2Se_3 features as a drawback the slow charge carriers transfer at the Sb_2Se_3|electrolyte interface, which is one of the limiting factors in obtaining a high-performance solar-driven HER [22]. As recently reported in our previous works, the charge carriers transfer for HER can be enhanced via modifying the surface of Sb_2Se_3 films with MoS_x- and Pt-based electrocatalysts [23,24]. Another issue that Sb_2Se_3 has is that the film surface of this material can be extremely hydrophobic, which considerably compromises the PEC performance of the material for H_2 generation via light-driven water splitting. The hydrophobic surface of Sb_2Se_3 stands as an issue for light-driven water splitting reaction, as it prevents water molecules or hydronium (H_3O^+) species from reaching the semiconductor's surface to be reduced by its photogenerated electrons. Therefore, semiconductor films featuring a hydrophilic surface is a fundamental prerequisite for the occurrence of the subsequent steps of light-driven water splitting. Materials presenting adequate roughness and surface energy can also directly contribute to the enhancement of the material's surface wettability since the presence of nano- or microstructures significantly contributes to high hydrophilicity [25,26].

It has been shown that surface wettability can be improved by exposing the materials to plasma [26–28], which is an electrically neutral substance comprised of electrons, neutrons, ions, free radicals, and excited particles [27]. In addition, exposing materials to a plasma environment enables a variety of surface modifications, such as structural reconstruction [29,30], surface etching to introduce defects [31], regulation of the vacancy's formation [32], and modulation of the band structure to improve wettability and conductivity [33], and all these surface modifications favored improvement of (photo)electrocatalytic activity for the oxygen evolution reaction, i.e., water oxidation. Another advantage of plasma treatment is that can also improve the electrocatalytic activity of the electrocatalysts for HER [31,32,34,35]. Regarding the plasma treatment of Sb_2Se_3 films for the sake of improving their wettability characteristic and photoelectroactivity for the HER, to the best of our knowledge, such an approach has not been attempted yet. Nevertheless, recent studies have shown the capability of dinitrogen (N_2) plasma treatment to improve wettability and photoelectroactivity for HER of antimony(III) sulfide (Sb_2S_3) films [36,37]. In this context, de Araújo and Mascaro [36] reported a novel N_2 plasma treatment approach to enhance H_2 generation on Sb_2S_3 thin films via light-driven water splitting. The PEC analyses showed that the plasma-treated Sb_2S_3 films delivered a substantial increase in j_{ph} value for HER of 24-fold compared to that of the untreated films, and this improvement was assigned to the enhanced wettability performance of the films (i.e., it changed from superhydrophobic, before plasma treatment, to hydrophilic, after plasma treatment). The enhanced wettability was due to the superficial chemical modification of the films, namely, the formation of an S−N polar group on the films surface by the N_2 plasma treatment.

In the present work, we propose a similar approach based on plasma treatment of the Sb_2Se_3 films to improve their wettability behavior and photoelectroactivity for H_2 generation via light-driven water splitting. Particularly, we aimed to evaluate the photoelectroactivity for HER of the Sb_2Se_3 films treated under N_2 and ambient air plasmas and subjected to different exposure times of these plasmas. As will be shown, the maximum j_{ph} value for HER was achieved for the N_2 plasma treatment, which delivered a value of approximately –3.9 mA cm^{-2} at −0.2 V_{RHE}. This value represented a 3-fold increase of the j_{ph} compared to that of the untreated film. To explain the substantial enhancement achieved of PEC performance for HER of the plasma-treated Sb_2Se_3 films, it was carried out a thorough physical and chemical characterization as well as an in-depth investigation of the wettability characteristics of the films. The results indicated that the enhanced PEC performance towards HER was due to the joint contribution of the improvement of surface wettability and the enlarged electrochemical active surface area (ECSA) of the plasma-treated Sb_2Se_3 films. At last, using a plasma treatment approach, in addition to considering a new surface modification strategy, provides a huge advantage over other techniques, such as being easy to handle, simple to reproduce, and able to operate with many samples at once. Thus, it can be used to improve the wettability of other semiconductor films and to enhance the PEC activity in aqueous medium.

2. Material and methods

2.1. Deposition of Sb_2Se_3 films

The detailed method of Sb_2Se_3 synthesis can be found elsewhere [23]. Briefly, it was employed a three-electrode cell configuration for the electrodeposition of Sb_2Se_3 films on FTO substrates, which were previously cleaned and hydrophilized. The counter electrode was a Pt plate (geometric area of ca. 1 cm^2), while the reference electrode was an Ag/AgCl/$Cl^-_{(sat.\ KCl)}$ and all the potential values presented in the text are referenced against the Ag/AgCl/$Cl^-_{(sat.\ KCl)}$ scale, unless the reversible hydrogen electrode (RHE) scale is specified. The films were obtained by potentiostatic co-electrodeposition at −0.60 V with a cutoff charge density of 600 mC cm^{-2}. The deposition bath was comprised of 2.0 mmol/L SeO_2 and 1.25 mmol/L $C_8H_4K_2O_{12}Sb_2{\cdot}xH_2O$ precursor solutions dissolved in the supporting electrolyte (i.e., 0.5 mol/L Na_2SO_4/H_2SO_4 at pH 2). Before the electrodeposition, this deposition bath was deaerated for 15 min with N_2 flow and maintained throughout the experiment as an atmosphere inside the cell. The electrodeposited films were subjected to thermal treatment at 300 ℃ for 60 min with a heating rate of 10 ℃ min^{-1} and under argon flux in a tubular furnace containing ≈ 200 mg of Se. The estimation of the thickness of the Sb_2Se_3 films (after the thermal treatment process) was ≈ 600 nm, as shown in Fig. S1. We should mention that was not possible to determine exactly the thickness of the films due to non-uniformity.

2.2. Plasma treatment of Sb_2Se_3 films

The plasma treatment of the Sb_2Se_3 films was performed in a commercial plasma cleaning machine (Zhengzhou CY-P2L-B) having an inner chamber size of 100 mm (diameter) and 270 mm (length), which corresponds to a volume of 2 L. The Sb_2Se_3 films were treated under plasma of N_2 (Sb_2Se_3(N_2-P)) and ambient air (Sb_2Se_3(air-P)) for 10, 20, and 30 s. The Sb_2Se_3 films treated under N_2 plasma for 10, 20 and 30 s were labeled as Sb_2Se_3(10 N_2-P), Sb_2Se_3(20 N_2-P) and Sb_2Se_3(30 N_2-P), respectively, and the Sb_2Se_3 films treated under ambient air plasma for 10, 20 and 30 s were designated as Sb_2Se_3(10 air-P), Sb_2Se_3(20 air-P) and Sb_2Se_3(30 air-P), respectively. The sample not subjected to plasma treatment (Sb_2Se_3(non-P)) was employed for comparison. Either the N_2 or ambient air plasma was generated by the application of a radio frequency (RF) of 13.56 MHz and RF power of 5 W. It was maintained a pressure of 30–35 Pa and gas flow of ca. 500 mL min^{-1} during the entire plasma treatment process. It is worth mentioning that the choice of these values provides the basis of plasma generation and was experimentally

determined by simplicity based on the etching capability of the plasma (i.e., removal of Sb_2Se_3 films from the substrate). Any increase in these parameter values could result in the total etching/removal of Sb_2Se_3 from its film's surface or even preventing the plasma generation. To guarantee reproducibility and control in all the experiments, the optimized parameters for plasma generation were employed for the plasma treatment of all the samples.

2.3. Pt deposition on Sb_2Se_3 films

It was deposited Pt nanoparticles over the untreated and plasma-treated Sb_2Se_3 films aiming to facilitate HER occurrence and minimize the photocorrosion process during the PEC experiments, as shown in our previous work [23]. Concerning the deposition procedure of Pt, 1.0 mmol/L $H_2PtCl_6{\cdot}xH_2O$ dissolved in the supporting electrolyte (i.e., 0.1 mol/L phosphate buffer solution (PBS) at pH 6.5) was used as Pt precursor. The deposition was performed using a three-electrode cell with a quartz window with the counter electrode and reference electrode being the same as previously mentioned [23], and the working electrode was the untreated and plasma-treated Sb_2Se_3 films. The electrodeposition of Pt nanoparticles was carried out under a solar light simulator (100 mW cm^{-2}, xenon lamp, and AM1.5G filter) and applying potentiostatically −0.1 V until reaching a deposition charge density of 60 mC cm^{-2}.

To better describe the different steps involved in the preparation of the photoelectrodes, a schematic representation is depicted in Fig. S2.

2.4. Physical and chemical characterization of the films

The crystalline structure of the films was characterized using an X-ray diffractometer (Rigaku DMax2500PC) with Cu $K\alpha_1$ radiation of 1.54 Å and a scan speed of 0.02° s^{-1}, in a range between $2\theta = 10$ to 60°. It was also characterized the vibrational modes of the materials employing a confocal Raman microscope (Horiba) with a 532 nm excitation laser. The films' chemical characterization was performed with an X-ray photoelectron spectrometer (Scienta Omicron ESCA 2SR) having the Al $K\alpha$ radiation (1486.7 eV) as the excitation source. To correct/minimize the surface charging effect, the binding energy value of all the spectra was adjusted by setting the C 1 s peak at 284.5 eV [38]. For the spectra fitting, it was employed the Gaussian-Lorentzian function (30 %) for peak adjustment, and the Tougaard function for the background. The chemical composition of the films was also assessed using a field emission scanning electron microscope (FE-SEM, Jeol JSM-7200F) equipped with an energy-dispersive X-ray spectrometer (Bruker XFlash 6|60 detector). The Morphological characterization was performed using a FE-SEM (Jeol JSM-7200F) operating at 15.0 kV. The optical characterization was accomplished using an ultraviolet–visible-near-infrared (UV-vis-NIR) spectrophotometer (Cary 5E) containing an integrating sphere for collection and measurement of diffusely reflected light signal. The value for α was determined using the Kubelka-Munk equation and E_g was obtained from Tauc extrapolation [39]. Besides the estimation of the optical E_g, it was also obtained the light-harvesting efficiency (LHE, elsewhere called "absorptance") of the films from the reflectance spectra, disregarding transmittance (for opaque objects), and employing the Equations (1) and (2) [40,41]. Static contact angle measurements on the film surface were performed using a goniometer (Ramé-hart 260 F4) and employing the sessile drop method. It was used water and diiodomethane as polar and apolar solvents, respectively. The topographical characterization of the films was carried out on an atomic force microscope (CSInstruments Nano-Observer) in contact mode.

$$\mathrm{LHE} = 1 - 10^{-A} \tag{1}$$

$$A = \log\frac{1}{R} \tag{2}$$

where A is the absorbance and R is the reflectance.

2.5. Photoelectrochemical characterization of the films

The PEC measurements were carried out in the same three-electrode cell with a quartz window that was described before. The counter and the reference electrodes were a Pt plate and an Ag/AgCl/$Cl^-_{(sat.\ KCl)}$, respectively. The working electrode was the untreated and plasma-treated Sb_2Se_3 films containing Pt nanoparticles on their surfaces. It was used 0.1 mol/L PBS at pH 6.5 as a supporting electrolyte in all PEC measurements. The potential values originally recorded against the Ag/AgCl/$Cl^-_{(sat.\ KCl)}$ scale were converted to the RHE scale (cf. Equation (3)) to facilitate comparison with the studies in the literature.

$$E\,(\mathrm{vs\ RHE}) = E\,(\mathrm{vs\ Ag/AgCl/Cl^-_{(sat.\ KCl)}}) + (\mathrm{pH} \times 0.059\ \mathrm{V}) + 0.197\ \mathrm{V} \tag{3}$$

where E (vs RHE) is the potential against the RHE scale, E (vs Ag/AgCl/$Cl^-_{(sat.\ KCl)}$) is the potential against the Ag/AgCl/$Cl^-_{(sat.\ KCl)}$ scale, and pH is the hydrogenionic potential of the supporting electrolyte (6.5).

The j_{ph} values were obtained from linear sweep voltammetry (LSV) at a scan rate (υ) of 5 mV s^{-1} and under chopped solar light simulation (100 mW cm^{-2}) with 3 s pulses for each light on and light off condition. The LSVs were obtained from the open-circuit potential to −0.4 V_{RHE}. Chronoamperometry measurements were performed to evaluate the short-time stability of the films via applying −0.2 V_{RHE} for 720 s under chopped illumination (60 s for each light on and off condition). It was also carried out photovoltage (V_{ph}) measurements of the films at open-circuited voltage (V_{oc}) conditions during 180 s and under chopped illumination (60 s for each light on and off condition). All the light pulses (i.e., light on and off) were controlled by an external device (shutter) coupled to the potentiostat/galvanostat. The V_{ph} experiments were performed in a two-electrode cell configuration with a quartz window. The working electrode was the untreated and plasma-treated Sb_2Se_3 films, and the counter electrode was a Pt plate.

3. Results and discussion

Initially, we employed scanning electron microscopy (SEM) and energy-dispersive X-ray spectroscopy (EDS) to evaluate the morphology and chemical composition, respectively, of the Sb_2Se_3 films treated under different plasma types and plasma treatment times (see Fig. 1a–g). For the Sb_2Se_3(non-P) film, it was noted the formation of globular clusters (Fig. 1a), which is a characteristic morphology for Sb_2Se_3 thin films obtained by co-electrodeposition followed by thermal treatment under sublimated Se atmosphere [11,24]. The globular clusters featured different lengths (the maximum one was approximately 1 μm) and were uniformly distributed over the entire film. Another aspect of these structures is the uniform distribution of Sb and Se elements, as shown by the EDS elemental mapping found below the SEM micrograph of Fig. 1a.

Regarding the plasma-treated films, Fig. 1b–d shows the surface of Sb_2Se_3 films treated under N_2 plasma at different exposure times. For the lowest N_2 plasma treatment time (i.e., 10 s), it is possible to notice that the Sb_2Se_3 clusters underwent an etching process, i.e., material removal from the film's surface (see Fig. 1b), and such a phenomenon becomes more evident for the N_2 plasma treatment of 20 s (cf. Fig. 1c). For the longest time of exposure to N_2 plasma (i.e., 30 s), one notices considerable etching of the Sb_2Se_3 clusters (see Fig. 1d), as at some portions these clusters were removed by the plasma action, revealing thus the tetrahedron-like structure characteristic of FTO substrate (for a better viewing see Fig. S3a). The occurrence of etching might have been the result of the bombardment of plasma species against the film surface with high enough kinetic energy [42] to eject atoms of Sb_2Se_3 films. Moreover, the ejection of material by the plasma bombardment has been widely documented in the literature for a variety of selenide-based compounds [43–45]. Concerning the chemical composition of the N_2 plasma-treated films, in addition to the presence of Sb and Se, the elemental mapping by EDS indicated the presence of N distributed uniformly over the films of Sb_2Se_3(20 N_2-P) and Sb_2Se_3(30 N_2-P) (cf.

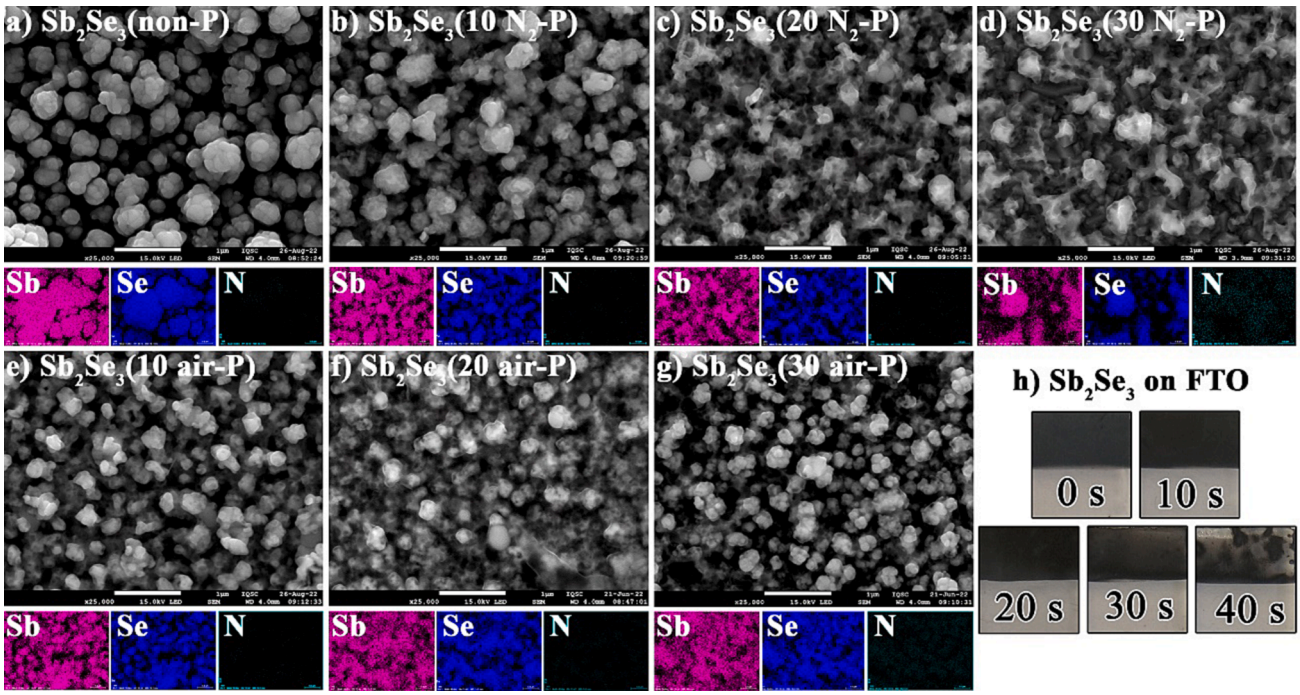

Fig. 1. a-g) FEG-SEM micrographs with a magnification of 25k times for untreated and plasma-treated Sb_2Se_3 films subjected to different plasma types and plasma treatment times. EDS elemental mapping of Sb, Se, and N are displayed below the corresponding FEG-SEM micrographs. h) Photographs of untreated and plasma-treated Sb_2Se_3 films subjected to different plasma treatment times.

Fig. 1c–d). In terms of atomic nitrogen percentage, it reached up to 4.3 % for the Sb_2Se_3(30 N_2-P) film (Fig. S4d).

For the films treated under ambient air plasma (Fig. 1e–g), it was also possible to verify from the EDS elemental mapping the presence of N for the longest plasma exposure time conditions (i.e., 20 and 30 s) and the maximum estimation of atomic nitrogen percentage was 1.1 % (see

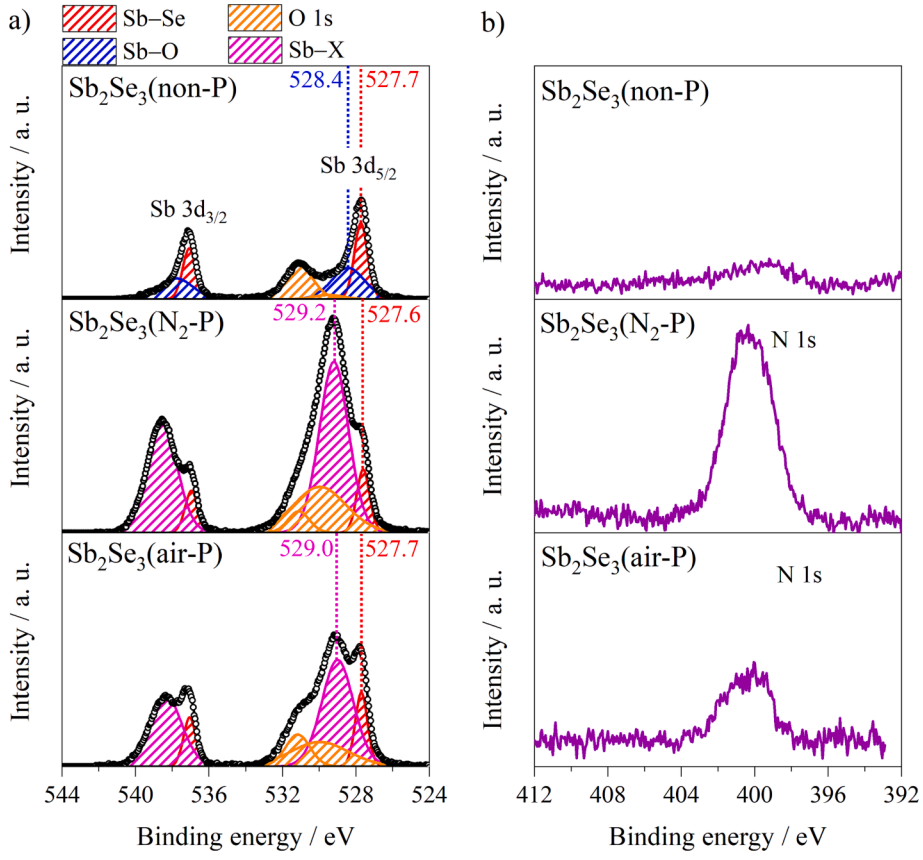

Fig. 2. High-resolution XPS spectra of a) Sb 3d and b) N 1 s core levels for untreated and plasma-treated Sb_2Se_3 films subjected to different plasma types for 10 s.

Fig. S4g). Concerning the morphology analysis, the ambient air plasma also led to etching the Sb_2Se_3 clusters. Compared with the same exposure times, ambient air plasma seems to be less aggressive than N_2 plasma as the Sb_2Se_3 clusters are less etched due to the bombardment of plasma species. Additionally, the Sb_2Se_3(30 air-P) film did not display exposed regions of FTO (see Fig. S3b), suggesting that the bombardment of ambient air plasma species may not have high enough kinetic energy to eject a large number of atoms of the Sb_2Se_3 film. The ejection of material from the Sb_2Se_3 films becomes even more obvious for plasma treatment time higher than 30 s. This can be observed for the film treated under plasma for 40 s which resulted in a substantial removal of the Sb_2Se_3 film from the FTO substrate, as shown by the photographs in Fig. 1h.

The untreated and plasma-treated Sb_2Se_3 films for 10 s under different plasma types were chemically assessed by high-resolution X-ray photoelectron spectroscopy (XPS), as shown in Fig. 2. Initially considering the XPS spectrum of the Sb_2Se_3(non-P) film (cf. Fig. 2a), one notices the presence of one doublet with the peaks of 527.7 and 537.04 eV, which corresponds to the Sb $3d_{5/2}$ and Sb $3d_{3/2}$ core levels, respectively, of the Sb–Se bonding of Sb_2Se_3. It was also noted another doublet with peaks of 528.4 and 537.74 eV that are characteristics of Sb $3d_{5/2}$ and Sb $3d_{3/2}$ core levels, respectively, and both are assigned to the Sb–O bound [46,47]. The additional peak located at 531.1 eV was assigned to the O 1 s and is probably attributed to the superficial oxidation of Sb_2Se_3. For the Sb_2Se_3(N_2-P) film, in addition to the doublet assigned to Sb–Se bonding of Sb_2Se_3, the XPS spectrum shows an additional doublet located at 529.2 eV (Sb $3d_{5/2}$) and 538.54 eV (Sb $3d_{3/2}$), which is probably associated with the formation of a new bond, namely Sb–N bond [48], that could have been arisen from the exchange of Se^{2-} ions for N^{3-} during the N_2 plasma treatment. The formation of Sb–N bond in the Sb_2Se_3(N_2-P) film can be verified in the N 1 s spectrum (cf. Fig. 2b), which displays a peak at ≈ 400 eV assigned to the occurrence of Sb–N [49]. The N 1 s spectrum of the untreated Sb_2Se_3 film did not display any photoemission peak of the Sb–N bond and this result verifies once again that the formation of Sb–N in the Sb_2Se_3 films only occurs during the N_2 plasma treatment. It is important to mention that given the close binding energy values of Sb–N and Sb–O bonds and the overlapping of O 1 s peak with the peak assigned possibly to Sb–N (see Fig. 2a), it is difficult to accurately assign the presence of Sb–N in the Sb 3d spectra for the plasma-treated films. Therefore, we have designated as Sb–X, which represents the occurrence of Sb–N and Sb–O in the plasma-treated films. Another important aspect to mention is that the mechanism involving Sb–N bond formation on the surface of Sb_2Se_3 films during nitrogen-based plasma treatment has not been investigated yet. However, based on reported studies for other materials [50], we believe that the fundamental steps involved are probably Sb–Se bond break and Sb–N bond formation on the Sb_2Se_3 films' surface due to the bombardment of highly energetic nitrogen ions of the plasma towards the films' surface. Additionally, the formation of metal–N bond under nitrogen-based plasma treatment has also been reported for other chalcogenide materials [35,51–54]. Although more studies would be required, these works indicate that the formation of this bond might have a possible tendency to occur in chalcogenide-based materials exposed to nitrogen plasma. Regarding the Sb 3d spectrum of the Sb_2Se_3(air-P) film (Fig. 2a), it was also observed the doublet located at 529.0 eV (Sb $3d_{5/2}$) and 538.3 eV (Sb $3d_{3/2}$) assigned to Sb–N bond and this bond formation can be confirmed by the presence of the photoemission peak in the N 1 s spectrum (cf. Fig. 2b), which is also associated to the occurrence of Sb–N bond [49]. Additionally, the doublet and the photoemission peak of the Sb 3d and N 1 s spectra, respectively, assigned to the Sb–N bond featured lower intensity for the Sb_2Se_3(air-P) film compared to that of the Sb_2Se_3(N_2-P) film. This reduction of peaks intensity may be associated with the fact that air in the earth's atmosphere has only ≈ 78 % N_2 in its composition [55], indicating that less N–based bonds are present on the film surface of the Sb_2Se_3(air-P). Another interesting feature of the XPS spectra for the plasma-treated Sb_2Se_3 films is the presence of O 1 s peaks, which might be attributed to the chemisorption of oxygen species on the surface of the film when exposed to atmospheric air [56]. Additionally, since the O 1 s components associated with the Sb–O bond undergo minimal changes after treatment with plasma of N_2 and ambient air, the modification on the surfaces of the films is mostly associated with the Sb–N bond. The presence of Sb–N bonds on Sb_2Se_3 films' surface plays an important role in the wettability improvement of Sb_2Se_3 films and consequently their PEC activity for H_2 generation from solar-driven water splitting, as will be shown in the discussion of Figs. 4 and 5, respectively.

The crystal structure characterization of the untreated (Sb_2Se_3(non-P)) and plasma-treated (Sb_2Se_3(N_2-P) and Sb_2Se_3(air-P)) films was assessed by X-ray diffraction (XRD) patterns and can be seen in Fig. 3a. Initially considering the Sb_2Se_3(non-P) film, the diffraction peaks without labels were indexed to the crystalline planes of the orthorhombic Sb_2Se_3 phase, which follows the standard patterns of the Powder Diffraction File (PDF) no. 89–821 [57] for Sb_2Se_3. The diffraction peaks labeled with asterisks (*) were assigned to SnO_2 (PDF no. 41–1445 [58]) from the FTO-coated glass substrates. For the plasma-treated samples, all the diffraction peaks without label were also indexed to the Sb_2Se_3 phase, no additional peaks concerning the formation of secondary phases have been identified. Additionally, as shown in Fig. S5, it has been observed a slight increase of the full width at half maximum (FWHM) values (corresponding to a percentage FWHM increase of around 10.5 %), suggesting that the crystal structure of the Sb_2Se_3 phase was affected during the plasma treatment. Specifically, treating the Sb_2Se_3 films under plasma of either N_2 or ambient air may have led to crystallographic stress in the Sb_2Se_3 crystal structure. The occurrence of this phenomenon may be linked to the shift of the main diffraction peak (corresponds to the (221) lattice plane) of the plasma-treated Sb_2Se_3 films that shifted 0.12° towards higher 2θ values compared to that of the untreated films (cf. Fig. S5). The interplanar spacing of Sb_2Se_3(N_2-P) and Sb_2Se_3(air-P) films also underwent reduction compared to that of the Sb_2Se_3(non-P) film. According to the Bragg's equation (cf. Equation (4), the interplanar distance of the (221) lattice plane, i.e., corresponding to the main diffraction peak, reduced from 0.2828 nm (Sb_2Se_3(non-P) film) to 0.2819 nm (Sb_2Se_3(N_2-P) and Sb_2Se_3(air-P) films), indicating a possible insertion of nitrogen atoms inside the crystal lattice of Sb_2Se_3 (the nitrogen atomic radii is smaller than that of selenium atom [59]). Similar results in terms of structural changes observed by XRD data were reported in the literature for other materials doped with nitrogen atoms via using N_2 plasma and magnetron sputtering under N_2 [60,61].

$$2d_{hkl}\sin\theta = \lambda \tag{4}$$

where d_{hkl} is the interplanar spacing of Sb_2Se_3 crystal, θ is the incident angle of the X-ray beam, and λ is the wavelength of the incident X-ray radiation (0.154056 nm).

Additional characterization of the untreated and plasma-treated Sb_2Se_3 films was achieved via the Raman spectra, as shown in Fig. 3b–d. For the Sb_2Se_3(non-P) film, the Raman spectrum (see Fig. 3b) displayed bands centered at 118, 189, and 210 cm^{-1}, and such bands are commonly attributed to the vibrational A_g modes of Sb_2Se_3 [62]. The band located at 118 cm^{-1} is assigned to the Se–Sb–Se bending [63,64], and the ones at 189 and 210 cm^{-1} are attributed to the Sb−Se−Sb bending [65,66]. The band centered at 254 cm^{-1} is assigned to the Sb_2O_3 secondary phase [63] and it has already been reported in other works as being only superficial [67–69]. Its formation may have been the result of different phenomena, such as: (i) the partial oxidation of the Sb_2Se_3 due to air exposure after synthesis and/or (ii) the energy delivered by the laser exposure during Raman measurements performed in air that could have led to the partial decomposition of Sb_2Se_3 into Sb_2O_3 [63]. It is interesting to note that the phase of Sb_2O_3 observed from the Raman spectrum was not identified in the XRD measurements (see Fig. 3a), and this may be linked to the differences in the sensibility of the

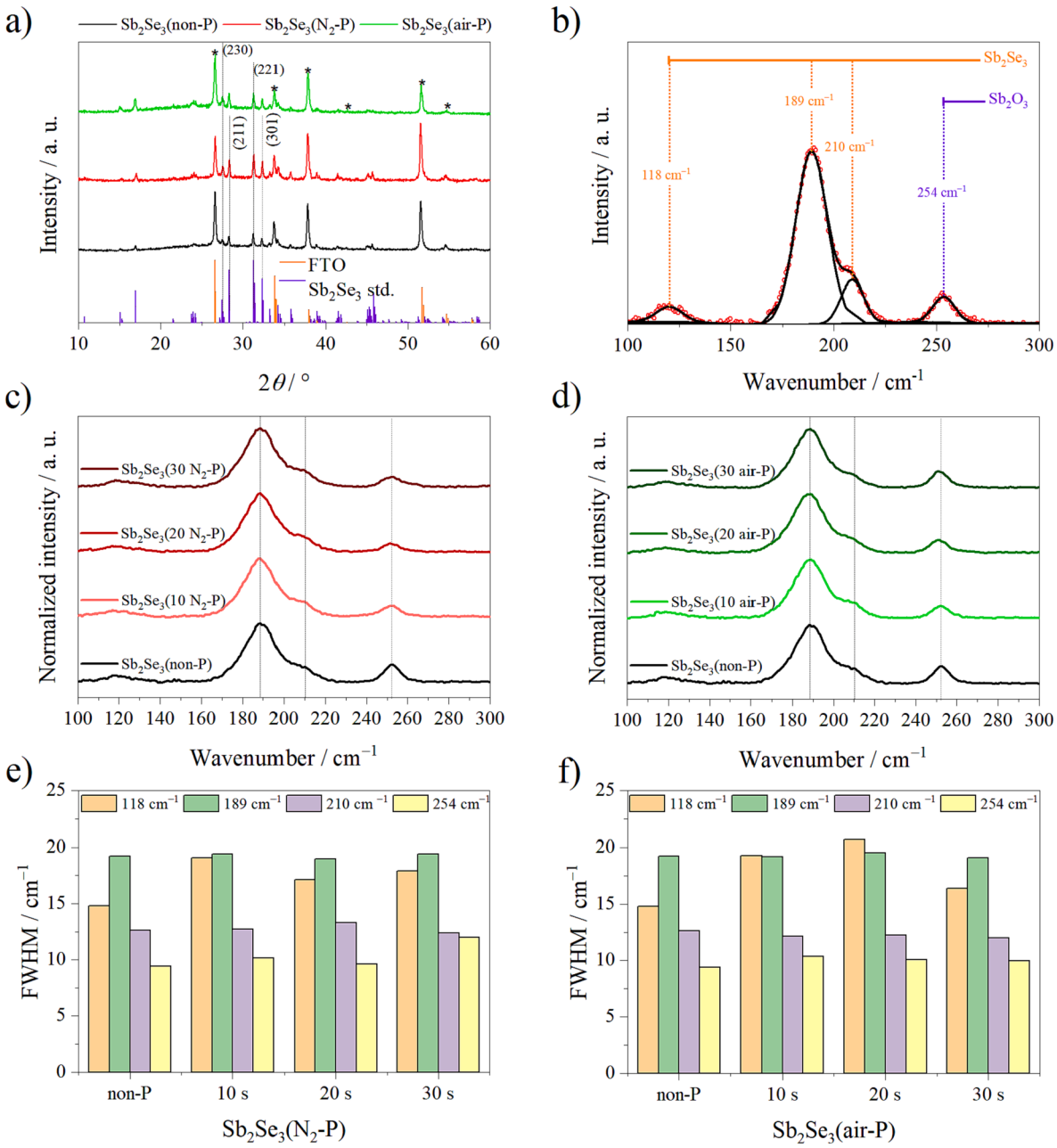

Fig. 3. a) XRD patterns for sb_2Se_3(non-P) and plasma-treated films ($Sb_2Se_3(N_2$-P) and Sb_2Se_3(air-P)) for 10 s. Standard patterns of the PDF database for Sb_2Se_3 (PDF no. 89–821 [57]) and SnO_2 (PDF no. 41–1445 [58]) phases are also displayed as vertical lines at the bottom of the diffractograms. Raman spectra for b) Sb_2Se_3(non-P), c) $Sb_2Se_3(N_2$-P), and d) Sb_2Se_3(air-P) films subjected to different plasma treatment times. FWHM values for e) $Sb_2Se_3(N_2$-P) and f) Sb_2Se_3(air-P) films subjected to plasma treatment at different times.

Raman and XRD techniques, such as vertical and/or lateral resolution [70].

Fig. 3c–d show the Raman spectra of the Sb_2Se_3 films treated under plasma of N_2 and ambient air, respectively, at different times. As noted, the Raman spectra of the plasma-treated films also displayed the characteristic bands of the Sb_2Se_3 phase, and it was not noticed additional bands, meaning that there is no formation of secondary phases upon plasma treatment. Aiming a further understanding of the plasma treatment effect on the crystal structure of the Sb_2Se_3 films, it was obtained the FWHM values of the Raman spectra for the untreated and plasma-treated Sb_2Se_3 films (see the values in Table S1). For such an analysis, Raman data processing employed spline and Gaussian functions to generate the baseline (which was subsequently subtracted) and the components of the bands, respectively. The intensity of the bands was normalized to the band centered at 189 cm^{-1}, which is the most intense band for Sb_2Se_3.

For the Sb_2Se_3(air-P) films (Fig. 3f), a noticeable variation of the FWHM values was only observed for the band at 118 cm^{-1} of the Sb_2Se_3 phase, whose values featured initially a gradual increase for the plasma treatment time 10 s (19.3 cm^{-1}) and 20 s (20.7 cm^{-1}) compared to that of the Sb_2Se_3(non-P) film (14.8 cm^{-1}). This behavior follows the XRD data, as the FWHM of the main diffraction peak also featured an increase for the plasma-treated films compared to that of the untreated one (cf. Fig. S5). Concerning the longest plasma treatment time, namely 30 s, the FWHM from the Raman spectrum underwent a reduction of its values (16.4 cm^{-1}) compared to the other plasma treatment times, however, it was still higher in comparison to the FWHM values for the untreated film. A similar trend was also observed for the FWHM values of the band

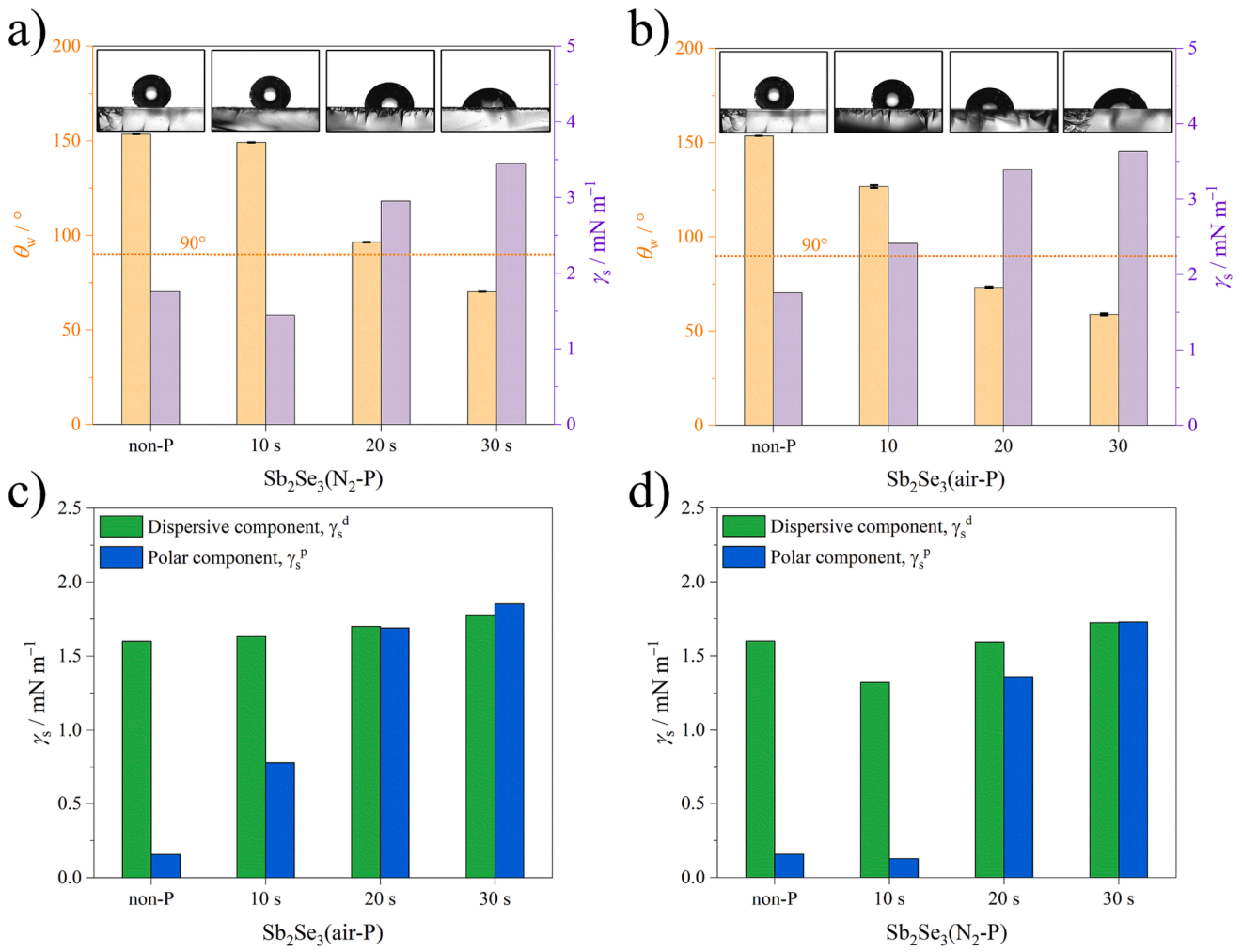

Fig. 4. a-b) θ_w and c-d) γ_s values for the untreated and plasma-treated Sb_2Se_3 films subjected to different plasma types and plasma treatment times.

at 189 cm^{-1} for the Sb_2Se_3(N_2-P) films (cf. Fig. 3e and Table S1). Compared to the untreated Sb_2Se_3 film, there was an initial increase of the FWHM value (up to 19.0 cm^{-1} for plasma treatment time of 10 s) followed by a decline (17.1 and 17.9 cm^{-1} for plasma exposure times of 20 and 30 s, respectively). It is believed that the initial increase of the FWHM value could be associated with the crystallographic stress by the insertion of the nitrogen atoms in the crystal lattice of Sb_2Se_3, as seen in the XRD data. Regarding the reduction of the FWHM values for the Sb_2Se_3(30 air-P), Sb_2Se_3(20 N_2-P), and Sb_2Se_3(30 N_2-P) films, we believe this might be linked to the partial or complete removal, i.e., etching effect by the plasma treatment, of the modified Sb_2Se_3 phase, namely Sb_2Se_3 phase containing probably incorporated nitrogen atoms and Sb–N bond formation on the Sb_2Se_3 surface.

To assess the optical properties of the Sb_2Se_3 films, the E_g of an indirect (allowed) electronic transition was estimated via the Tauc plots for Sb_2Se_3(N_2-P) and Sb_2Se_3(air-P) films (Figs. S6a–b, respectively) subjected to different plasma treatment times. The E_g for the Sb_2Se_3(-non-P) film was ca. 1.18 eV, which closely agrees with the value reported in the literature [47,71,72]. The plasma-treated Sb_2Se_3 films did not show a substantial change in the E_g values, indicating that plasma treatment does not affect significantly the optical properties of the Sb_2Se_3 films. Despite these E_g values being relatively close compared to the Sb_2Se_3(non-P) film, the small variations of E_g may be linked to the occurrence of chemical defects such as vacancies, which could have originated from the plasma etching effect [44]. We have also investigated the effect of plasma treatment on the light absorption ability of the Sb_2Se_3 films and for this, it was obtained the LHE plots, as shown in Figs. S6c-d. The LHE of the Sb_2Se_3(non-P) film reached a considerable value of up to 0.95 in the range of 800 and 950 nm. For the plasma-treated Sb_2Se_3 films, the LHE values did not alter significantly compared to that of the untreated film, which suggests that the plasma treatment does not have a substantial influence on the light absorption capability of the Sb_2Se_3 films.

To have a full picture of the light-driven water splitting process, it is primally important to understand how a photoelectrode surface and a liquid interact as well as how such an interaction pertains to the water splitting performance. To verify these, wettability tests were performed for the untreated and plasma-treated Sb_2Se_3 films and the results are shown in Fig. 4. Before evaluating the results, it is important to keep in mind that wettability can be defined as the tendency of a liquid to spread over a flat rigid solid surface [73]. In a microscopic domain, wettability can be delineated as a property governed by intermolecular interactions to portray the extent of wetting of a solid rigid surface by a liquid droplet [74]. Typically, wettability can be described in terms of static contact angle determined by tangential angle that originates from the balance of the surface tensions among the solid–vapor, liquid–vapor, and solid–liquid interfaces. It is generally accepted that a solid surface is characterized as hydrophobic when its static water contact angle (θ_w) is higher than 90° and is hydrophilic when this angle is lower than 90° [75]. These wettability parameters play a fundamental role in the application of semiconductor thin films for solar-driven water splitting since the semiconductor|electrolyte interface must present a hydrophilic behavior.

Having in mind all these aforementioned concepts, the θ_w was

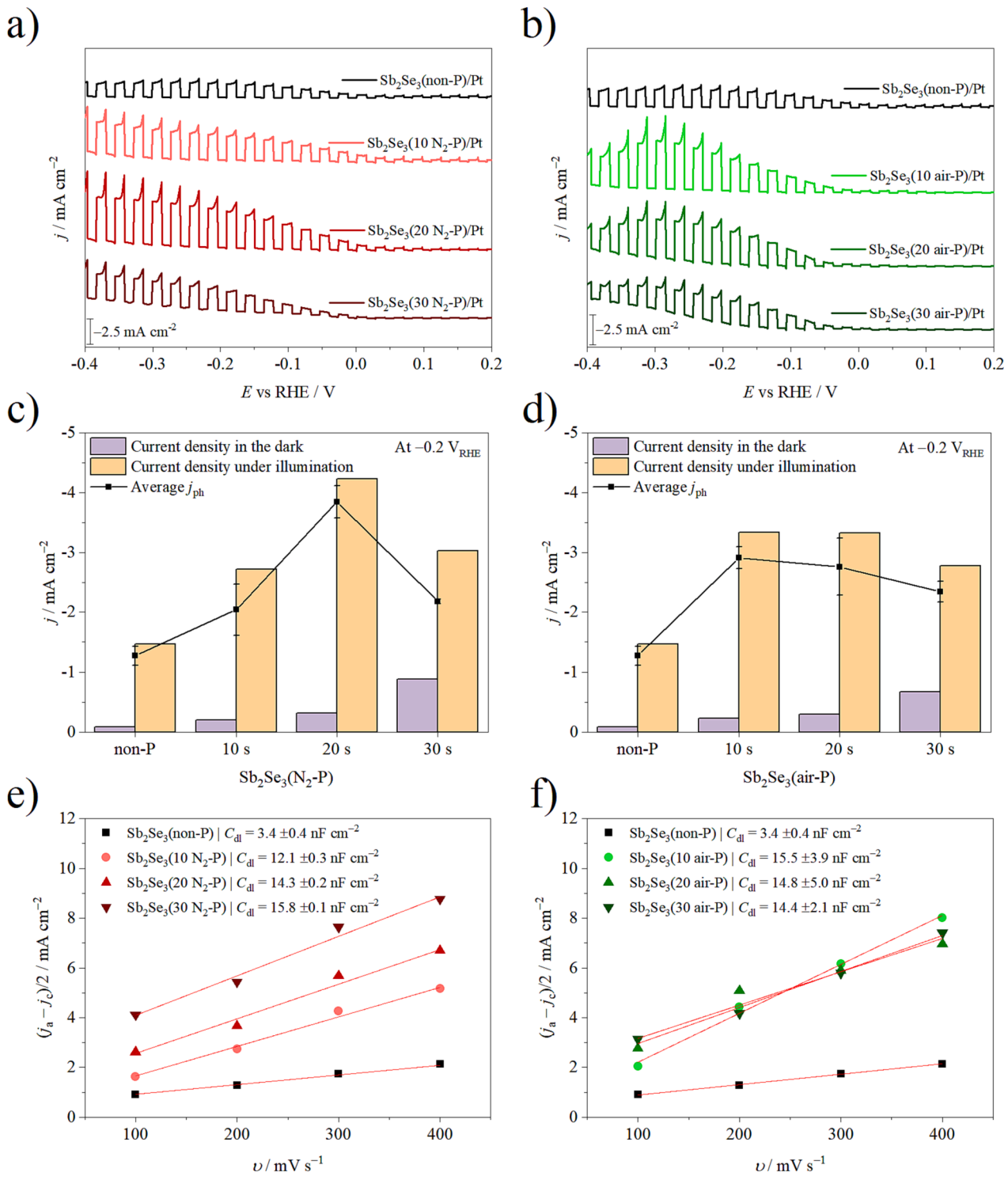

Fig. 5. a–b) LSV at a υ of 5 mV s^{-1} and under chopped illumination (100 mW cm^{-2}), c–d) current density in the dark, current density under illumination and average j_{ph} values at −0.2 V_{RHE}, and e–f) $(j_a - j_c)/2$ vs υ plots of untreated and plasma-treated Sb_2Se_3 films subjected to different plasma types and plasma treatment times. The electrolyte was an N_2-saturated solution of 0.1 mol/L PBS (pH 6.5).

determined for the $Sb_2Se_3(N_2\text{-P})$ and Sb_2Se_3(air-P) films subjected to different plasma treatment times, as shown in Fig. 4a–b, respectively. The θ_w of the untreated Sb_2Se_3 film is also displayed in both figures for the sake of comparison. The surface of Sb_2Se_3(non-P) film showed $\theta_w >$ 90°, indicating that the film surface features low wettability or hydrophobic behavior [76]. For the plasma-treated films, the θ_w values decreased over the plasma treatment time. For the $Sb_2Se_3(N_2\text{-P})$ films, only the film treated for 30 s showed $\theta_w <$ 90°, meaning a high wettability or hydrophilicity of this film surface. On the other hand, the Sb_2Se_3(air-P) films treated for 20 and 30 s featured θ_w below this limit of 90°, which is once again characteristic of the hydrophilic surface. The wettability improvement for the plasma-treated films might be linked to the presence of Sb–N bonds on the Sb_2Se_3 films' surface (cf. discussion of Fig. 2), as the N in the Sb–N bond tends to form hydrogen bonds with water molecules [77].

The origin of the hydrophobicity of the Sb_2Se_3 is related to its crystal

growth orientation and the presence of dangling bonds exposed on the Sb_2Se_3 films surface. According to Kim et al. [78], the hydrophilic/phobic capacity of the Sb_2Se_3 surface is directly linked to the preferential orientation of its 1D ribbon-like orthorhombic crystal structure. The crystal structure of Sb_2Se_3 is comprised of ribbons that contain Sb and Se atoms strongly bounded by covalent bonds along the [0 0 1] direction, while these ribbon-like structures are stacked in parallel by van der Waals forces [12]. Thus, (00l) planes have a large number of dangling bonds formed by breaking the Sb−Se bonds of the ribbon-like structures which can be found on the surface of the Sb_2Se_3 film. These dangling bonds can contribute to the increase in the surface energy of the (00l) planes of the Sb_2Se_3 and consequently increase its hydrophilicity, which in turn means that the adhesive forces between the Sb_2Se_3 surface and the water droplet become stronger than the cohesive forces of the water molecules [78]. On the other hand, the (*h*00) and (0*k*0) planes exposed on the surface of Sb_2Se_3 do not have dangling bonds and therefore, contribute to the hydrophobic character of the semiconductor [78].

The wettability behavior of the plasma-treated films was further evaluated in terms of solid surface tension (γ_s), also known as surface free energy, which was estimated based on the Fowkes method [79], i.e., taking into consideration the contribution of the dispersive component (γ_s^d) and the polar component (γ_s^p) of the solid surface tension, as shown in Equations (5)–(8) [80–82].

$$\gamma_s = \gamma_s^d + \gamma_s^p \tag{5}$$

$$\gamma_{lv}(1+\cos\theta) = 2\left(\sqrt{\gamma_s^d\gamma_{lv}^d} + \sqrt{\gamma_s^p\gamma_{lv}^p}\right) \tag{6}$$

$$\gamma_s^d = \frac{\gamma_{lv,dm}(1+\cos\theta_{dm})^2}{4} \tag{7}$$

$$\gamma_s^p = \frac{\left(\gamma_{lv,w}(1+\cos\theta_w) - 2\sqrt{\gamma_s^d\gamma_{lv,w}^d}\right)^2}{4\gamma_{lv,w}^p} \tag{8}$$

where γ_{lv} is the interfacial surface tension of the liquid–vapor interface in which the liquid can be water ($\gamma_{lv,w}$ = 72.8 mN m^{-1}) or diiodomethane ($\gamma_{lv,dm}$ = 50.8 mN m^{-1}), θ is the static contact angle of the water (θ_w) or diiodomethane (θ_{dm}), γ_{lv}^d is the dispersive component of the interfacial liquid–vapor tension in which the liquid can be water ($\gamma_{lv,w}^d$ = 21.8 mN m^{-1}) or diiodomethane ($\gamma_{lv,dm}^d$ = 50.8 mN m^{-1}), and γ_{lv}^p is the polar component of the interfacial liquid–vapor tension in which the liquid can be water ($\gamma_{lv,w}^p$ = 51 mN m^{-1}) or diiodomethane ($\gamma_{lv,dm}^p$ = 0 mN m^{-1}) [83].

The γ_s values estimated by employing Equations (5)–(8) and the average θ_w and θ_{dm} values (cf. Table S2) are compiled in Fig. 4a–b for Sb_2Se_3(N_2-P) and Sb_2Se_3(air-P) films, respectively, subjected to different plasma treatment times. Compared to the Sb_2Se_3(non-P) film, both Sb_2Se_3(N_2-P) and Sb_2Se_3(air-P) films displayed an increased tendency of the γ_s values over the plasma treatment times. This tendency can be better explained by the increase in the γ_s^p values (estimated via Equation (8) for both Sb_2Se_3(N_2-P) and Sb_2Se_3(air-P) films, as shown in Fig. 4c–d). Knowing that γ_s^p arises from permanent dipole–dipole interactions [84] or Keesom forces [85], the increased γ_s^p is linked to the introduction of nitrogen-containing polar functional groups on the surface of the films (as shown by the XPS data in Fig. 2) via the plasma treatment of either N_2 ambient air. The presence of the polar functional groups enables greater attraction of water molecules towards the surface of the plasma-treated films due to the predominance of adhesive forces (i.e., forces that act on attracting water molecules onto the photoelectrode surface). Such a hypothesis is based on the improvement of the wettability characteristic of the plasma-treated films as noted by the continuous decrease of the θ_w values over plasma treatment times. It is also interesting to point out from Fig. 4c–d that the γ_s^d value (estimated via Equation (7) was higher than γ_s^p for Sb_2Se_3(non-P) film. Since γ_s^d pictures the induced dipole–dipole interactions (London-van der Waals forces or London dispersion forces) [84], the $\gamma_s^d > \gamma_s^p$ for the Sb_2Se_3(non-P) film suggests poor attraction of water molecules towards the film surface due to the cohesion force (i.e., the attraction of water molecules to each other) of water being the predominant one. This results in poor wettability behavior for the Sb_2Se_3(non-P) film, as observed by the $\theta_w > 90°$. Despite the γ_s^d did not significantly change for the plasma-treated films, the γ_s^p increased over plasma treatment times, suggesting enhancement of the films' surface adhesion with water (i.e., improvement of the ability of water molecules to be drawn to the surface of Sb_2Se_3 films), as shown by the $\theta_w < 90°$. Another interesting aspect noted from Fig. 4 is that the wettability behavior of the Sb_2Se_3 films treated under plasma of N_2 and ambient air were very similar and did not exhibit significant difference, even the XPS analyses showing different amounts of nitrogen atoms bonded on the surface of the films (cf. Fig. 2). The contact angle for water molecules may have achieved a saturation of wettability degree, regardless of the amount of Sb–N bounds present in the surface of Sb_2Se_3 films as shown in the XPS analyses.

At last, we have evaluated the effect of plasma type and plasma treatment time on the PEC activity of the plasma-treated Sb_2Se_3 films toward HER. As mentioned previously, to perform the PEC experiments, Pt nanoparticles were deposited on the surface of the untreated and plasma-treated Sb_2Se_3 films, as Pt hinders photocorrosion of Sb_2Se_3 films and facilitates the HER [23]. The surface modification of the plasma-treated films with Pt can be observed by the SEM images, which show the presence of small particles of Pt over the plasma-treated Sb_2Se_3 films (cf. Fig. S7). Additionally, based on EDS elemental mapping (see Fig. S8a), it was possible to confirm the presence of Pt distributed on the plasma-treated films. It was also estimated the amount of Pt photoelectrodeposited from the EDS spectrum, and the atomic percentage of Pt was approximately 1.0 at.% (see Fig. S8b). Regarding the PEC performance of the plasma-treated Sb_2Se_3 films having Pt nanoparticles on their surface, Fig. 5a–b show the LSV measurements in a potential range between 0.2 V_{RHE} (approximately in the open circuit potential conditions) and –0.4 V_{RHE} for the Sb_2Se_3 films treated under plasma of N_2 and ambient air, respectively, at different plasma treatment times. Still concerning Fig. 5a–b, both untreated and plasma-treated Sb_2Se_3 films presented cathodic j_{ph} signal, as indicated by the negative value of the current density of the scale bar located at the base of the LSVs. This cathodic photoresponse is assigned to the solar-driven HER, since the conduction band edge potential of Sb_2Se_3 is more negative than the potential of HER [86], which means that the photogenerated electrons in the conduction band of Sb_2Se_3 can be transferred to reduce H_3O^+ or water to H_2. Fig. 5c–d show the current density values in the dark and under illumination, and their respective j_{ph} for HER at −0.2 V_{RHE} for Sb_2Se_3(N_2-P) and Sb_2Se_3(air-P) films, respectively, at different plasma treatment times.

For the Sb_2Se_3 films treated under N_2 plasma (Fig. 5a and 5c), it is possible to observe a trend of increase and decrease of the j_{ph} for HER as the plasma treatment time increases. It was achieved a maximum average j_{ph} value for HER of (–3.9 ± 0.3) mA cm^{-2} at −0.2 V_{RHE} for the Sb_2Se_3(20 N_2-P) film. This means that the j_{ph} value was 3-fold higher for the film treated under N_2 plasma during 20 s compared to that of the untreated film, whose value reached (–1.3 ± 0.2) mA cm^{-2} at −0.2 V_{RHE}. The improvement of photoresponse for HER may be due to the increase in the γ_s^p or, more specifically, the enhanced adhesion of water to the surface of the plasma-treated Sb_2Se_3 films, implying thus improvement of wettability or hydrophilic characteristic of the films, as observed by the reduction of the θ_w (see Fig. 4a–b). The occurrence of the hydrophilic surface for the plasma-treated films is probably related mainly to the surface modification of these films, i.e., the presence of the Sb–N bond (see discussion of Fig. 2) since the crystallographic stress caused by the insertion of N atoms (cf. Fig. S5) did not result in significant differences in the results regarding the bulk properties of the semiconductor. The presence of Sb–N bonds on the Sb_2Se_3 film surface may have contributed to the enhancement of wettability because the N

in the Sb–N bond is prone to forming hydrogen bonds with water molecules [77]. It is also important to highlight that the plasma-treated films presenting a hydrophilic surface can provide better adsorption of water or H_3O^+ species, which is a crucial process for the subsequent step of light-driven HER, namely photogenerated electron transfer at the semiconductor|electrolyte interface [87,88]. Additionally, the Sb_2Se_3 films featuring a hydrophilic surface by the plasma treatment can also reduce the size of the generated H_2 bubbles in contact with the photoelectrode surface [89], and this stands advantageously as it minimizes the blockage of the active surface sites of the films by the bubbles as well as diminish the probability of losses associated with the bubbles' presence, e.g., kinetic and ohmic losses, and optical losses [90]. In addition to the improvement of the j_{ph} signal for HER, it was noted a decline in the j_{ph} of the Sb_2Se_3 film treated for 30 s under N_2 plasma (see Fig. 5c), and this is mainly due to the etching of the film exposed to a long plasma treatment time (i.e., $\geq$ 30 s), which resulted, consequently, in the loss of the light absorber material. Another interesting feature noted from Fig. 5c is that the current density in the dark increased over plasma treatment time. This is an indication that the electron transfer for HER in the absence of illumination is also improved after plasma treatment of the films, nevertheless, the PEC performance of the films remained superior since all the plasma treatment conditions, as well as non-plasma conditions, delivered considerably higher current density values under illumination compared to those in the absence of illumination. Regarding the PEC performance of the films treated under plasma of ambient air (Fig. 5b and 5d), the maximum j_{ph} value for HER was achieved for the plasma treatment times of 10 and 20 s, which delivered a value of approximately –3 mA cm^{-2} at −0.2 V_{RHE}. This value represented a 2.3-fold increase of the j_{ph} compared to that of the untreated film, and this enhanced photoresponse is due to the improvement of water adhesion to the surface of the plasma-treated films, which favor the subsequent steps of HER, as discussed previously for the films treated N_2 plasma. Behaving in the same fashion as the films treated under N_2 plasma, the Sb_2Se_3 films treated under plasma of ambient air for 30 s, i.e., the longest plasma treatment time, displayed a decrease in the j_{ph} value compared to the other plasma treatment times (cf. Fig. 5d). This decline of j_{ph} is probably linked to the removal of Sb_2Se_3 material by the plasma of ambient air (i.e., etching effect), as discussed previously for the films treated with N_2 plasma. Furthermore, similar to the films treated under N_2 plasma, the current density in the dark of the films treated under ambient air plasma increased over the plasma treatment time.

Besides the assessment of the j_{ph} signal for HER, we have investigated the V_{ph} values of the untreated and plasma-treated films via the V_{oc} measurements under light off/light on conditions (cf. Fig. S9a). The investigation of V_{ph} was only performed for the films treated at the optimized exposure plasma time (i.e., 20 s for N_2 plasma and 10 s for ambient air plasma). For this analysis, it is important to bear in mind that the V_{ph} value reflects the magnitude of the quasi-Fermi level splitting of the electrons and holes of a semiconductor electrode under illumination [91]. Generally, semiconductors with higher V_{ph} values have larger E_g and, therefore, provide greater driving force for the reduction or oxidation of species in solution [92]. Concerning the obtained V_{ph} values, the plasma treatment has not resulted in a significant difference in the V_{ph} value of the plasma-treated films compared to that of the untreated film (cf. Fig. S9a), and this result is probably due to the E_g of the films that did not significantly change after plasma treatment (see Fig. S6a–b). In addition to the PEC activity evaluation (i.e., j_{ph} and V_{ph} for HER), we have also investigated the stability of the untreated and plasma-treated Sb_2Se_3 films via chronoamperometries measurements at –0.2 V_{RHE} during 720 s and under chopped illumination, as shown in Fig. S9b. The stability experiments were carried out for the films treated at the optimized exposure plasma time (i.e., 20 s for N_2 plasma and 10 s for ambient air plasma), and both untreated and plasma-treated films contained Pt nanoparticles deposited on their surface. According to Fig. S9b, for the analyzed range of time, the results show that the untreated and plasma-treated Sb_2Se_3 films remained stable under polarization and chopped illumination, which can be observed by the plateau region of the current density under illumination that kept practically constant over time. The observed stability for the untreated and plasma-treated films is linked to the presence of the Pt nanoparticles deposited on the films that acted as an electrocatalyst and kept the j_{ph} stable during the analyzed range of time, as reported in our previous work [23].

Aiming to have a better understanding of the PEC performance of the Sb_2Se_3 films treated under different plasma types and at different plasma treatment times, we have evaluated the ECSA from the double-layer capacitance density (C_{dl}) of the films, since the C_{dl} is directly proportional to the ECSA [93]. The C_{dl} value was calculated from the slope of the linear relationship of the $(j_a - j_c)/2$ vs υ (see Fig. 5e–f), where $(j_a - j_c)/2$ is half of the differences between anodic current density (j_a) and cathodic current density (j_c). The j_a and j_c values were obtained from cyclic voltammetry performed in the capacitive region (from –0.15 to –0.05 V) and at different υ (i.e., 100, 200, 300, and 400 mV s^{-1}), as shown in Fig. S10. According to Fig. 5e-f, the Sb_2Se_3(N_2-P) films showed changes in the C_{dl} values (ranging from 12.1 to 15.8 nF cm^{-2}) under different plasma exposure times, whereas the Sb_2Se_3(air-P) films did not show substantial changes in the C_{dl} values (the average was 14.9 nF cm^{-2}). These results suggest that the increase of N_2 plasma exposure time leads to the increase of the C_{dl} or ECSA of the plasma-treated films, and the different exposure times of ambient air plasma do not affect significantly the C_{dl} or ECSA of the plasma-treated films. Another important aspect to mention is that despite the Sb_2Se_3(30 N_2-P) film presented the highest ECSA value, the loss of semiconductor material during the N_2 plasma treatment (i.e., the etching effect) was a disadvantage to this film to achieve a better PEC performance. Regarding the effect of the plasma type, the films treated under plasma of N_2 and ambient air featured an increase of the C_{dl} values up to 4.6-fold compared to that of the untreated film (3.4 nF cm^{-2}), indicating that the treatment under both plasma types results in the increase of the ECSA. The increase of C_{dl} or ECSA of the plasma-treated films compared to that of the untreated film is probably due to the etching capability of the plasma that leads to an apparent rougher surface, as shown by the SEM micrographs (cf. Fig. 1a-g). Since is generally found that the increase of the roughness is directly proportional to the ECSA [94], the apparent rougher surface of the plasma-treated films may have led to a better PEC performance due to the larger surface area that enables a greater number of available active sites for the occurrence of the light-driven HER.

To verify that there has been an increase in the roughness of the plasma-treated films, it was employed AFM to obtain two-dimensional (2D) and three-dimensional (3D) images with a size of 5.0 μm × 5.0 μm of Sb_2Se_3(non-P), Sb_2Se_3(20 N_2-P), and Sb_2Se_3(10 air-P) films, as shown in Fig. S11. Based on the AFM data, the Sb_2Se_3(non-P), Sb_2Se_3(20 N_2-P), and Sb_2Se_3(10 air-P) films presented arithmetic averages roughness (R_a) of 0.92 ± 0.32, 2.53 ± 0.48, and 2.75 ± 0.95 nm, respectively, meaning that the surface of the untreated film was smoother compared to those of the plasma-treated films. The increased values of R_a confirm our hypothesis about the increase of ECSA for the plasma-treated films compared to that of the untreated films (cf. Fig. 5e–f) and that can be associated with the improved j_{ph} values (see Fig. 5c–d) for the HER. Another interesting feature of the R_a values obtained from Fig. S11 is that the error associated with the R_a value of the Sb_2Se_3(10 air-P) film was greater than the Sb_2Se_3(20 N_2-P) film (a similar trend was noticed from the error associated with the C_{dl} values, see Figures e-f). This result indicates a lower roughness possibility and hence a slight minor j_{ph} for the Sb_2Se_3(10 air-P) compared to that of the Sb_2Se_3(20 N_2-P) film.

As a final remark, on the strength of the experimental evidence presented, the improvement of surface wettability and the increase of the ECSA of the plasma-treated films may have jointly contributed to the improvement of the j_{ph} signal for HER.

4. Conclusions

To summarize, the employment of plasma treatment to semiconductor films of Sb_2Se_3 has proved to be an effective alternative approach to substantially improve the PEC performance of the films to produce H_2 via water splitting. The enhancement of PEC performance of the plasma-treated Sb_2Se_3 films has been associated with the improvement of surface wettability (i.e., hydrophilic characteristic) compared to the untreated film, whose surface was extremely hydrophobic. The hydrophilic surface of the plasma-treated films might be linked to the chemical modification of the films' surface, i.e., the presence of Sb–N bonds on the Sb_2Se_3 films surface that could have arisen during the plasma treatment of either N_2 or ambient air, as confirmed by the XPS analyses. The Sb–N bonds on the Sb_2Se_3 films surface may have contributed to the enhancement of wettability because the N in the Sb–N bond has the propensity to form hydrogen bonds with water molecules. The presence of N was also observed by the EDS elemental mapping, which showed N distributed evenly over the plasma-treated film surface. Additionally, N species may have been incorporated in the crystal lattice of Sb_2Se_3, nevertheless, this was a minority effect since only slight modifications were noticed from XRD and Raman data of the plasma-treated films compared to the untreated film. This means that the improvement of wettability of the plasma-treated films is mainly due to the superficial modification of the Sb_2Se_3 films. Besides enabling a hydrophilic surface, the plasma treatment of N_2 and ambient air have also resulted in the increase of roughness and ECSA of the Sb_2Se_3 films. Therefore, the enhancement of PEC response towards HER is assigned to the combined contribution of improved wettability and enlarged ECSA of the plasma-treated Sb_2Se_3 films. At last, the new contribution of this work is the surface modification strategy via plasma treatment to improve the wettability of semiconductor films, which is fundamentally crucial to enable PEC water splitting, as well as to enhance PEC activity towards H_2 generation.

CRediT authorship contribution statement

Magno B. Costa: Writing – original draft, Visualization, Validation, Methodology, Formal analysis, Data curation, Conceptualization. **Moisés A. de Araújo:** Writing – original draft, Visualization, Validation, Methodology, Investigation, Formal analysis, Data curation, Conceptualization. **Robert Paiva:** Writing – original draft, Validation, Methodology, Formal analysis, Data curation. **Sandra A. Cruz:** Validation, Supervision, Investigation, Formal analysis. **Lucia H. Mascaro:** Writing – review & editing, Supervision, Resources, Investigation, Funding acquisition, Formal analysis, Conceptualization.

Declaration of competing interest

The authors declare that they have no known competing financial interests or personal relationships that could have appeared to influence the work reported in this paper.

Data availability

Data will be made available on request.

Acknowledgments

This work was supported by the São Paulo Research Foundation (FAPESP) [grant numbers #2017/21365-8, #2016/12681-0, #2013/07296-2, and #2017/11986-5]; the Conselho Nacional de Desenvolvimento Científico e Tecnológico (CNPq) [grant numbers #152607/2022-6, #311769/2022-5, #406156/2022-0, and #405336/2022-5]; and Financiadora de Estudos e Projetos (FINEP) [grant numbers #01.22.0179.00and #0036/21]. This study was financed in part by the Coordenação de Aperfeiçoamento de Pessoal de Nível Superior - Brasil (CAPES) - Finance Code 001. The authors also thank Shell and the strategic importance of the support given by ANP (Brazil's National Oil, Natural Gas, and Biofuels Agency) through the R&D levy regulation.

We also would like to thank Dr. Sirlon Blaskievicz and MSc Gleison N. Marques, both from Universidade Federal de São Carlos (UFSCar), for obtaining the Raman spectra and the AFM images of the samples, respectively, and Prof. Dr. Valmor R. Mastelaro from Universidade de São Paulo (USP) for obtaining the XPS spectra of the samples.

Appendix A. Supplementary data

Supplementary data to this article can be found online at https://doi.org/10.1016/j.cej.2024.149526.

References

[1] M. Rashad, M. Daowd, A.M.A. Amin, A comparative study on photovoltaic and concentrated solar thermal power plants, Recent Advances in Environmental and Earth Sciences and Economics (2015) 167–173.
[2] S. Chen, T. Liu, Z. Zheng, M. Ishaq, G. Liang, P. Fan, T. Chen, J. Tang, Recent progress and perspectives on Sb2Se3-based photocathodes for solar hydrogen production via photoelectrochemical water splitting, Journal of Energy Chemistry 67 (2022) 508–523, https://doi.org/10.1016/j.jechem.2021.08.062.
[3] K. Zeng, D.-J. Xue, J. Tang, Antimony selenide thin-film solar cells, Semicond Sci Technol 31 (2016) 1–13, https://doi.org/10.1088/0268-1242/31/6/063001.
[4] J. Tan, W. Yang, Y. Oh, H. Lee, J. Park, J. Moon, Controlled Electrodeposition of Photoelectrochemically Active Amorphous MoS_x Cocatalyst on Sb_2Se_3 Photocathode, ACS Appl Mater Interfaces 10 (2018) 10898–10908, https://doi.org/10.1021/acsami.8b00305.
[5] C. Chen, W. Li, Y. Zhou, C. Chen, M. Luo, X. Liu, K. Zeng, B. Yang, C. Zhang, J. Han, J. Tang, Optical properties of amorphous and polycrystalline Sb_2Se_3 thin films prepared by thermal evaporation, Appl Phys Lett 107 (2015) 043905, https://doi.org/10.1063/1.4927741.
[6] C.E. Patrick, F. Giustino, Structural and electronic properties of semiconductor-sensitized solar-cell interfaces, Adv Funct Mater 21 (2011) 4663–4667, https://doi.org/10.1002/adfm.201101103.
[7] L. Zhang, Y. Li, C. Li, Q. Chen, Z. Zhen, X. Jiang, M. Zhong, F. Zhang, H. Zhu, Scalable low-band-gap Sb_2Se_3 thin-film photocathodes for efficient visible–near-infrared solar hydrogen evolution, ACS Nano 11 (2017) 12753–12763, https://doi.org/10.1021/acsnano.7b07512.
[8] J. Park, W. Yang, J. Tan, H. Lee, J.W. Yun, S.G. Shim, Y.S. Park, J. Moon, Hierarchal nanorod-derived bilayer strategy to enhance the photocurrent density of Sb_2Se_3 photocathodes for photoelectrochemical water splitting, ACS Energy Lett 5 (2020) 136–145, https://doi.org/10.1021/acsenergylett.9b02486.
[9] X. Liu, J. Chen, M. Luo, M. Leng, Z. Xia, Y. Zhou, S. Qin, D. Xue, L. Lv, H. Huang, D. Niu, J. Tang, Thermal Evaporation and Characterization of Sb_2Se_3 Thin Film for Substrate Sb_2Se_3/CdS Solar Cells, ACS Appl Mater Interfaces 6 (2014) 10687–10695, https://doi.org/10.1021/am502427s.
[10] Y. Zhou, M. Leng, Z. Xia, J. Zhong, H. Song, X. Liu, B. Yang, J. Zhang, J. Chen, K. Zhou, J. Han, Y. Cheng, J. Tang, Solution-processed antimony selenide heterojunction solar cells, Adv Energy Mater 4 (2014) 1301846, https://doi.org/10.1002/aenm.201301846.
[11] M.B. Costa, F.W. de Souza Lucas, L.H. Mascaro, Thermal treatment effects on electrodeposited Sb_2Se_3 photovoltaic Thin Films, ChemElectroChem 4 (2017) 2507–2514, https://doi.org/10.1002/celc.201700511.
[12] Y. Zhou, L. Wang, S. Chen, S. Qin, X. Liu, J. Chen, D.-J. Xue, M. Luo, Y. Cao, Y. Cheng, E.H. Sargent, J. Tang, Thin-film Sb_2Se_3 photovoltaics with oriented one-dimensional ribbons and benign grain boundaries, Nat Photonics 9 (2015) 409–415, https://doi.org/10.1038/nphoton.2015.78.
[13] C. Chen, D.C. Bobela, Y. Yang, S. Lu, K. Zeng, C. Ge, B. Yang, L. Gao, Y. Zhao, M. C. Beard, J. Tang, Characterization of basic physical properties of Sb_2Se_3 and its relevance for photovoltaics, Frontiers of Optoelectronics 10 (2017) 18–30, https://doi.org/10.1007/s12200-017-0702-z.
[14] G. Liang, M. Chen, M. Ishaq, X. Li, R. Tang, Z. Zheng, Z. Su, P. Fan, X. Zhang, S. Chen, Crystal growth promotion and defects healing enable minimum open-circuit voltage deficit in antimony selenide solar cells, Adv. Sci. 9 (2022), https://doi.org/10.1002/advs.202105142.
[15] G. Chen, Y. Luo, M. Abbas, M. Ishaq, Z. Zheng, S. Chen, Z. Su, X. Zhang, P. Fan, G. Liang, Suppressing buried interface nonradiative recombination losses toward high-efficiency antimony triselenide solar cells, Adv. Mater. (2023), https://doi.org/10.1002/adma.202308522.
[16] G. Liang, T. Liu, M. Ishaq, Z. Chen, R. Tang, Z. Zheng, Z. Su, P. Fan, X. Zhang, S. Chen, Heterojunction interface engineering enabling high onset potential in Sb_2Se_3/CdS photocathodes for efficient solar hydrogen production, Chem. Eng. J. 431 (2022) 133359, https://doi.org/10.1016/j.cej.2021.133359.
[17] S. Chen, T. Liu, M. Chen, M. Ishaq, R. Tang, Z. Zheng, Z. Su, X. Li, X. Qiao, P. Fan, G. Liang, Crystal growth promotion and interface optimization enable highly efficient Sb_2Se_3 photocathodes for solar hydrogen evolution, Nano Energy 99 (2022) 107417, https://doi.org/10.1016/j.nanoen.2022.107417.
[18] J. Lin, G. Chen, N. Ahmad, M. Ishaq, S. Chen, Z. Su, P. Fan, X. Zhang, Y. Zhang, G. Liang, Back contact interfacial modification mechanism in highly-efficient

antimony selenide thin-film solar cells, Journal of Energy Chemistry 80 (2023) 256–264, https://doi.org/10.1016/j.jechem.2023.01.049.
[19] S. Chen, Y. Fu, M. Ishaq, C. Li, D. Ren, Z. Su, X. Qiao, P. Fan, G. Liang, J. Tang, Carrier recombination suppression and transport enhancement enable high-performance self-powered broadband Sb2Se3 photodetectors, InfoMat 5 (2023), https://doi.org/10.1002/inf2.12400.
[20] R. Tang, S. Chen, Z. Zheng, Z. Su, J. Luo, P. Fan, X. Zhang, J. Tang, G. Liang, Heterojunction annealing enabling record open-circuit voltage in antimony triselenide solar cells, Adv. Mater. 34 (2022), https://doi.org/10.1002/adma.202109078.
[21] Y. Luo, G. Chen, S. Chen, N. Ahmad, M. Azam, Z. Zheng, Z. Su, M. Cathelinaud, H. Ma, Z. Chen, P. Fan, X. Zhang, G. Liang, Carrier transport enhancement mechanism in highly efficient antimony selenide thin-film solar cell, Adv Funct Mater 33 (2023), https://doi.org/10.1002/adfm.202213941.
[22] M.B. Costa, F.W.S. Lucas, L.H. Mascaro, Improvement of electrodeposited Sb_2Se_3 thin film photoelectroactivity by cobalt grain boundary modification, J Mater Chem A Mater (2020), https://doi.org/10.1039/D0TA03160G.
[23] M.V. de L. Tinoco, M.B. Costa, L.H. Mascaro, J.F. de Brito, Photoelectrodeposition of Pt nanoparticles on Sb_2Se_3 photocathodes for enhanced water splitting, Electrochim Acta 382 (2021) 138290, https://doi.org/10.1016/j.electacta.2021.138290.
[24] M.B. Costa, F.W. de S. Lucas, M. Medina, L.H. Mascaro, All-electrochemically-grown Sb_2Se_3/a-MoS_x Photocathode for Hydrogen Production: The Effect of the MoS_x Layer on the Surface Recombination and Photocorrosion of Sb_2Se_3 Films, ACS Appl Energy Mater (2020) acsaem.0c01413. https://doi.org/10.1021/acsaem.0c01413.
[25] B. Bhushan, Y.C. Jung, Micro- and nanoscale characterization of hydrophobic and hydrophilic leaf surfaces, Nanotechnology 17 (2006) 2758–2772, https://doi.org/10.1088/0957-4484/17/11/008.
[26] J.S.G. de Camargo, A.J. de Menezes, N.C. da Cruz, E.C. Rangel, A. de O. Delgado-Silva, Morphological and chemical effects of plasma treatment with oxygen (O2) and sulfur hexafluoride (SF6) on Cellulose Surface, Mater. Res. 20 (2018) 842–850, https://doi.org/10.1590/1980-5373-mr-2016-1111.
[27] Y. Luo, Y. Wu, C. Huang, C. Menon, S. Feng, P.K. Chu, Plasma modified and tailored defective electrocatalysts for water electrolysis and hydrogen fuel cells, EcoMat 4 (2022), https://doi.org/10.1002/eom2.12197.
[28] S. Zanini, C. Riccardi, M. Orlandi, V. Fornara, M.P. Colombini, D.I. Donato, S. Legnaioli, V. Palleschi, Wood coated with plasma-polymer for water repellence, Wood Sci Technol 42 (2008) 149–160, https://doi.org/10.1007/s00226-007-0160-7.
[29] Z. Liu, X. Wu, B. Zheng, Y. Sun, C. Hou, J. Wu, K. Huang, S. Feng, Cobalt-plasma treatment enables structural reconstruction of a CoO_x/$BiVO_4$ composite for efficient photoelectrochemical water splitting, Chem. Commun. (2022), https://doi.org/10.1039/D2CC03257K.
[30] G. Che, D. Wang, C. Wang, F. Yu, D. Li, N. Suzuki, C. Terashima, A. Fujishima, Y. Liu, X. Zhang, Solution plasma boosts facet-dependent photoactivity of decahedral $BiVO_4$, Chem. Eng. J. 397 (2020) 125381, https://doi.org/10.1016/j.cej.2020.125381.
[31] D. Yan, R. Chen, Z. Xiao, S. Wang, Engineering the electronic structure of Co_3O_4 by carbon-doping for efficient overall water splitting, Electrochim Acta 303 (2019) 316–322, https://doi.org/10.1016/j.electacta.2019.02.091.
[32] J.H. Lin, Y.T. Yan, T.X. Xu, C.Q. Qu, J. Li, J. Cao, J.C. Feng, J.L. Qi, S doped $NiCo_2O_4$ nanosheet arrays by Ar plasma: an efficient and bifunctional electrode for overall water splitting, J Colloid Interface Sci 560 (2020) 34–39, https://doi.org/10.1016/j.jcis.2019.10.056.
[33] T. Ma, S. Jin, X. Kong, M. Lv, H. Wang, X. Luo, H. Tan, Z. Li, Y. Zhang, X. Chang, X. Song, Plasma engraved Bi_2MoO_6 nanosheet arrays towards high performance supercapacitor and oxygen evolution reaction, Appl Surf Sci 548 (2021) 149244, https://doi.org/10.1016/j.apsusc.2021.149244.
[34] P.-C. Huang, S. Brahma, P.-Y. Liu, J.-L. Huang, S.-C. Wang, S.-C. Weng, M. Shaikh, Atmospheric air plasma treated SnS films: an efficient electrocatalyst for HER, Catalysts 8 (2018) 462, https://doi.org/10.3390/catal8100462.
[35] A.D. Nguyen, T.K. Nguyen, C.T. Le, S. Kim, F. Ullah, Y. Lee, S. Lee, K. Kim, D. Lee, S. Park, J.-S. Bae, J.I. Jang, Y.S. Kim, Nitrogen-plasma-treated continuous monolayer MoS_2 for improving hydrogen evolution reaction, ACS Omega 4 (2019) 21509–21515, https://doi.org/10.1021/acsomega.9b03205.
[36] M.A. Araújo, L.H. Mascaro, Plasma treatment: a novel approach to improve the photoelectroactivity of thin films to water splitting, ChemElectroChem 7 (2020) 2325–2329, https://doi.org/10.1002/celc.202000496.
[37] M.A. de Araújo, M.B. Costa, L.H. Mascaro, Improved photoelectrochemical hydrogen gas generation on Sb_2S_3 films modified with an earth-abundant MoS_x Co-Catalyst, ACS Appl Energy Mater 5 (2022) 1010–1022, https://doi.org/10.1021/acsaem.1c03374.
[38] J.F. Moulder, W.F. Stickle, P.E. Sobol, K.D. Bomben, Handbook of X-ray Photoelectron Spectroscopy, 2nd ed., Perkin-Elmer Corporation, Eden Prairie, 1992.
[39] M.G. Walter, E.L. Warren, J.R. McKone, S.W. Boettcher, Q. Mi, E.A. Santori, N. S. Lewis, Solar water splitting cells, Chem Rev 110 (2010) 6446–6473, https://doi.org/10.1021/cr1002326.
[40] Q. Wu, J. Hou, H. Zhao, Z. Liu, X. Yue, S. Peng, H. Cao, Charge recombination control for high efficiency CdS/CdSe quantum dot co-sensitized solar cells with multi-ZnS layers, Dalton Trans. 47 (2018) 2214–2221, https://doi.org/10.1039/C7DT04356B.
[41] Z. Chen, H.N. Dinh, E. Miller, Photoelectrochemical Water Splitting: Standards, Experimental Methods, and Protocols, 1st ed., Springer-Verlag New York, New York, 2013.
[42] B. Bhushan, ed., Encyclopedia of Nanotechnology, Springer Netherlands, Dordrecht, 2012. https://doi.org/10.1007/978-90-481-9751-4.
[43] A.T. Barton, L.A. Walsh, C.M. Smyth, X. Qin, R. Addou, C. Cormier, P.K. Hurley, R. M. Wallace, C.L. Hinkle, Impact of etch processes on the chemistry and surface states of the topological insulator Bi_2Se_3, ACS Appl Mater Interfaces 11 (2019) 32144–32150, https://doi.org/10.1021/acsami.9b10625.
[44] D. Xiao, Q. Ruan, D. Bao, Y. Luo, C. Huang, S. Tang, J. Shen, C. Cheng, P.K. Chu, Effects of ion energy and density on the plasma etching-induced surface area, edge electrical field, and multivacancies in MoSe2 nanosheets for enhancement of the hydrogen evolution reaction, Small 16 (2020) 2001470, https://doi.org/10.1002/smll.202001470.
[45] M. Tosun, L. Chan, M. Amani, T. Roy, G.H. Ahn, P. Taheri, C. Carraro, J.W. Ager, R. Maboudian, A. Javey, Air-stable n-doping of WSe_2 by anion vacancy formation with mild plasma treatment, ACS Nano 10 (2016) 6853–6860, https://doi.org/10.1021/acsnano.6b02521.
[46] L. Bodenes, A. Darwiche, L. Monconduit, H. Martinez, The Solid Electrolyte Interphase a key parameter of the high performance of Sb in sodium-ion batteries: comparative X-ray photoelectron spectroscopy study of Sb/Na-ion and Sb/Li-ion batteries, J Power Sources 273 (2015) 14–24, https://doi.org/10.1016/j.jpowsour.2014.09.037.
[47] A. Mavlonov, T. Razykov, F. Raziq, J. Gan, J. Chantana, Y. Kawano, T. Nishimura, H. Wei, A. Zakutayev, T. Minemoto, X. Zu, S. Li, L. Qiao, A review of Sb_2Se_3 photovoltaic absorber materials and thin-film solar cells, Sol. Energy 201 (2020) 227–246, https://doi.org/10.1016/j.solener.2020.03.009.
[48] C.P. Thao, T.T.A. Tuan, D.-H. Kuo, W.-C. Ke, T.T.V.S. Na, Reactively sputtered Sb-GaN films and its hetero-junction diode: the exploration of the n-to-p transition, Coatings 10 (2020) 210, https://doi.org/10.3390/coatings10030210.
[49] Q. Sun, W.-J. Li, Z.-W. Fu, A novel anode material of antimony nitride for rechargeable lithium batteries, Solid State Sci 12 (2010) 397–403, https://doi.org/10.1016/j.solidstatesciences.2009.12.003.
[50] S. Samipour, H. Taghvaei, D. Mohebbi-Kalhori, M.R. Rahimpour, Plasma treatment and chitosan coating: a combination for improving PET surface properties, Surf Innov 8 (2020) 76–88, https://doi.org/10.1680/jsuin.19.00030.
[51] C. Guorong, H. Zheng, X. Jun, C. Jijian, Surface modification of chalcogenide glasses by N_2 plasma treatment, J Non Cryst Solids 288 (2001) 226–229, https://doi.org/10.1016/S0022-3093(01)00642-1.
[52] A. Azcatl, X. Qin, A. Prakash, C. Zhang, L. Cheng, Q. Wang, N. Lu, M.J. Kim, J. Kim, K. Cho, R. Addou, C.L. Hinkle, J. Appenzeller, R.M. Wallace, Covalent nitrogen doping and compressive strain in MoS_2 by Remote N_2 Plasma Exposure, Nano Lett 16 (2016) 5437–5443, https://doi.org/10.1021/acs.nanolett.6b01853.
[53] J. Jiang, Q. Zhang, A. Wang, Y. Zhang, F. Meng, C. Zhang, X. Feng, Y. Feng, L. Gu, H. Liu, L. Han, A facile and effective method for patching sulfur vacancies of WS_2 via nitrogen plasma treatment, Small 15 (2019), https://doi.org/10.1002/smll.201901791.
[54] L. Zhang, L. Feng, P. Li, X. Chen, Y. Gao, Y. Gong, Z. Du, S. Zhang, A. Zhang, G. Chen, H. Wang, Plasma-assisted doping of nitrogen into cobalt sulfide for loading cadmium sulfide: a direct Z-scheme heterojunction for efficiently photocatalytic Cr(VI) reduction under visible light, Chem. Eng. J. 417 (2021) 129222, https://doi.org/10.1016/j.cej.2021.129222.
[55] E. Glueckauf, The Composition of Atmospheric Air, in: Compendium of Meteorology, American Meteorological Society, Boston, MA, 1951: pp. 3–10. https://doi.org/10.1007/978-1-940033-70-9_1.
[56] Z. Ma, H. Hou, K. Song, Z. Fang, L. Wang, F. Gao, W. Yang, B. Tang, Y. Kuang, Engineering oxygen vacancies by one-step growth of distributed homojunctions to enhance charge separation for efficient photoelectrochemical water splitting, Chem. Eng. J. 379 (2020) 122266, https://doi.org/10.1016/j.cej.2019.122266.
[57] M. Min, J. Zhai, X. Wang, B. Shen, G. Wen, T. Fan, Refinement of the crystal structure for a new mineral —antimonselite, Chin. Sci. Bull. 43 (1998) 413–416, https://doi.org/10.1007/BF02883722.
[58] G.J. McCarthy, J.M. Welton, X-ray diffraction data for SnO2 an illustration of the new powder data evaluation methods, Powder Diffr 4 (1989) 156–159, https://doi.org/10.1017/S0885715600016638.
[59] E. Clementi, D.L. Raimondi, W.P. Reinhardt, Atomic Screening Constants from SCF Functions. II. Atoms with 37 to 86 Electrons, J Chem Phys 47 (1967) 1300–1307, https://doi.org/10.1063/1.1712084.
[60] E. Aperathitis, M. Modreanu, M. Bender, V. Cimalla, G. Ecke, M. Androulidaki, N. Pelekanos, Optical characterization of indium-tin-oxynitride fabricated by RF-sputtering, Thin Solid Films 450 (2004) 101–104, https://doi.org/10.1016/j.tsf.2003.10.046.
[61] L. Tian, G. Cheng, H. Wang, Y. Wu, R. Zheng, P. Ding, Effect of nitrogen doping on the structural, optical and electrical properties of indium tin oxide films prepared by magnetron sputtering for gallium nitride light emitting diodes, Superlattices Microstruct 101 (2017) 261–270, https://doi.org/10.1016/j.spmi.2016.11.054.
[62] N. Fleck, T.D.C. Hobson, C.N. Savory, J. Buckeridge, T.D. Veal, M.R. Correia, D. O. Scanlon, K. Durose, F. Jäckel, Identifying Raman modes of Sb_2Se_3 and their symmetries using angle-resolved polarised Raman spectra, J Mater Chem A Mater 8 (2020) 8337–8344, https://doi.org/10.1039/D0TA01783C.
[63] A. Shongalova, M.R. Correia, B. Vermang, J.M.V. Cunha, P.M.P. Salomé, P. A. Fernandes, On the identification of Sb_2Se_3 using Raman scattering, MRS Commun 8 (2018) 1–6, https://doi.org/10.1557/mrc.2018.94.
[64] I. Efthimiopoulos, J. Zhang, M. Kucway, C. Park, R.C. Ewing, Y. Wang, Sb_2Se_3 under pressure, Sci Rep 3 (2013) 2665, https://doi.org/10.1038/srep02665.
[65] G. Li, Z. Li, J. Chen, X. Chen, S. Qiao, S. Wang, Y. Xu, Y. Mai, Self-powered, high-speed Sb_2Se_3/Si heterojunction photodetector with close spaced sublimation processed Sb_2Se_3 layer, J Alloys Compd 737 (2018) 67–73, https://doi.org/10.1016/j.jallcom.2017.12.039.

[66] A. Kumar, V. Kumar, A. Romeo, C. Wiemer, G. Mariotto, Raman Spectroscopy and in situ XRD probing of the thermal decomposition of Sb_2Se_3 Thin Films, J. Phys. Chem. C 125 (2021) 19858–19865, https://doi.org/10.1021/acs.jpcc.1c05047.
[67] M. Luo, M. Leng, X. Liu, J. Chen, C. Chen, S. Qin, J. Tang, Thermal evaporation and characterization of superstrate CdS/Sb_2Se_3 solar cells, Appl Phys Lett 104 (2014), https://doi.org/10.1063/1.4874878.
[68] A.K. Jain, C. Gopalakrishnan, P. Malar, Study of pulsed laser deposited antimony selenide thin films, J. Mater. Sci. Mater. Electron. 33 (2022) 10430–10438, https://doi.org/10.1007/s10854-022-08030-1.
[69] S. Wen, X. Yin, H. Xie, Y. Guo, J. Liu, D. Liu, W. Que, H. Liu, W. Liu, Vapor transport deposition of Sb_2Se_3 thin films for photodetector application, J Adv Dielectr 10 (2020) 2050016, https://doi.org/10.1142/S2010135X20500162.
[70] K. Miyoshi, Surface Characterization Techniques: An Overview, in: Mechanical Tribology, 1st ed., CRC Press, Boca Raton, 2004: p. 24.
[71] R. Vadapoo, S. Krishnan, H. Yilmaz, C. Marin, Electronic structure of antimony selenide (Sb2Se3) from GW calculations, Physica Status Solidi (b) 248 (2011) 700–705, https://doi.org/10.1002/pssb.201046225.
[72] X. Liu, Y. Qiao, Y. Liu, J. Liu, E. Jia, S. Chang, X. Shen, S. Li, K. Cheng, Enhanced open circuit voltage of Sb_2Se_3/CdS solar cells by annealing Se-rich amorphous Sb_2Se_3 films prepared via sputtering process, Sol. Energy 195 (2020) 697–702, https://doi.org/10.1016/j.solener.2019.11.072.
[73] A. Fujinami, D. Matsunaka, Y. Shibutani, Water wettability/non-wettability of polymer materials by molecular orbital studies, Polymer (guildf) 50 (2009) 716–720, https://doi.org/10.1016/j.polymer.2008.11.050.
[74] N. Slepickova Kasalkova, P. Slepicka, Z. Kolska, V. Svorcik, Wettability and Other Surface Properties of Modified Polymers, in: Wetting and Wettability, InTech, 2015. https://doi.org/10.5772/60824.
[75] K.-Y. Law, Water–surface interactions and definitions for hydrophilicity, hydrophobicity and superhydrophobicity, Pure Appl. Chem. 87 (2015) 759–765, https://doi.org/10.1515/pac-2014-1206.
[76] K.-Y. Law, Definitions for hydrophilicity hydrophobicity, and superhydrophobicity: getting the basics right, J Phys Chem Lett 5 (2014) 686–688, https://doi.org/10.1021/jz402762h.
[77] P. Muller, Glossary of terms used in physical organic chemistry (IUPAC Recommendations 1994), Pure Appl. Chem. 66 (1994) 1077–1184, https://doi.org/10.1351/pac199466051077.
[78] Y.B. Kim, S.W. Cho, N.G. Deshpande, S.H. Jung, D.S. Kim, K.J. Park, H. Kim, H. K. Cho, Smart bifunctional Sb_2Se_3 nanorods for integrated water purification: insoluble liquid separation and photoelectrochemical degradation, ChemSusChem 13 (2020) 3017–3027, https://doi.org/10.1002/cssc.202000438.
[79] F.M. Fowkes, Calculation of work of adhesion by pair potential suummation, J Colloid Interface Sci 28 (1968) 493–505, https://doi.org/10.1016/0021-9797(68)90082-9.
[80] C.-F. Wang, D.D. Ejeta, J.-Y. Wu, S.-W. Kuo, C.-H. Lin, J.-Y. Lai, Tuning the wettability and surface free energy of poly(vinylphenol) thin films by modulating hydrogen-bonding interactions, Polymers (basel) 12 (2020) 523, https://doi.org/10.3390/polym12030523.
[81] D.Y. Kwok, D. Li, A.W. Neumann, Fowkes' surface tension component approach revisited, Colloids Surf A Physicochem Eng Asp 89 (1994) 181–191, https://doi.org/10.1016/0927-7757(94)80117-7.
[82] F.M. Fowkes, Attractive forces at interfaces, Ind Eng Chem 56 (1964) 40–52, https://doi.org/10.1021/ie50660a008.
[83] R.J. Good, C.J. van Oss, The Modern Theory of Contact Angles and the Hydrogen Bond Components of Surface Energies, in: M.E. Schrader, G.I. Loeb (Eds.), Modern Approaches to Wettability: Theory and Applications, 1st ed., Springer, New York, 1992.
[84] M. Annamalai, K. Gopinadhan, S.A. Han, S. Saha, H.J. Park, E.B. Cho, B. Kumar, A. Patra, S.-W. Kim, T. Venkatesan, Surface energy and wettability of van der Waals structures, Nanoscale 8 (2016) 5764–5770, https://doi.org/10.1039/C5NR06705G.
[85] W.H. Keesom, The second viral coefficient for rigid spherical molecules, whose mutual attraction is equivalent to that of a quadruplet placed at their centre, Royal Netherlands Academy of Arts and Sciences, Proceeding 18 (1915) 636–646.
[86] W. Yang, J. Moon, Recent advances in earth-abundant photocathodes for photoelectrochemical water splitting, ChemSusChem 12 (2019) 1889–1899, https://doi.org/10.1002/cssc.201801554.
[87] H. Kim, J. Park, I. Park, K. Jin, S.E. Jerng, S.H. Kim, K.T. Nam, K. Kang, Coordination tuning of cobalt phosphates towards efficient water oxidation catalyst, Nat Commun 6 (2015) 8253, https://doi.org/10.1038/ncomms9253.
[88] Y. Li, C. Zhao, Enhancing Water Oxidation Catalysis on a Synergistic Phosphorylated NiFe Hydroxide by Adjusting Catalyst Wettability, ACS Catal 7 (2017) 2535–2541, https://doi.org/10.1021/acscatal.6b03497.
[89] C. Meng, B. Wang, Z. Gao, Z. Liu, Q. Zhang, J. Zhai, Insight into the role of surface wettability in electrocatalytic hydrogen evolution reactions using light-sensitive nanotubular TiO_2 Supported Pt Electrodes, Sci Rep 7 (2017) 41825, https://doi.org/10.1038/srep41825.
[90] A. Bhanawat, K. Zhu, L. Pilon, How do bubbles affect light absorption in photoelectrodes for solar water splitting? Sustain Energy Fuels 6 (2022) 910–924, https://doi.org/10.1039/D1SE01730F.
[91] M. Grätzel, Photoelectrochemical cells, Nature 414 (2001) 338–344, https://doi.org/10.1038/35104607.
[92] R.G.S. Pala, Should all electrochemical energy materials be isomaterially heterostructured to optimize contra and co-varying physicochemical properties? Front Chem 8 (2020) https://doi.org/10.3389/fchem.2020.00515.
[93] H.Q. Fu, L. Zhang, C.W. Wang, L.R. Zheng, P.F. Liu, H.G. Yang, 1D/1D hierarchical nickel sulfide/phosphide nanostructures for electrocatalytic water oxidation, ACS Energy Lett 3 (2018) 2021–2029, https://doi.org/10.1021/acsenergylett.8b00982.
[94] D. Coelho, G. Luiz, S. Machado, Estimating the electrochemically active area: revisiting a basic concept in electrochemistry, J Braz Chem Soc (2021), https://doi.org/10.21577/0103-5053.20210080.